PCCP

Why does B2O3 suppress nepheline (NaAlSiO 4) crystallization in sodium aluminosilicate glasses?

Journal:	*Physical Chemistry Chemical Physics*
Manuscript ID	CP-ART-01-2020-000172.R1
Article Type:	Paper
Date Submitted by the Author:	14-Mar-2020
Complete List of Authors:	Deshkar, Ambar ; Rutgers The State University of New Jersey, Materials Science & Engineering Gulbiten, Ozgur; Corning Inc, Science & Technology Division Yougman, Randall; Corning Inc, Science & Technology Division Mauro, John; Pennsylvania State University, Goel, Ashutosh; Rutgers, The State University of New Jersey,

Why does B_2O_3 suppress nepheline ($NaAlSiO_4$) crystallization in sodium aluminosilicate glasses?

Ambar Deshkar,[1] Ozgur Gulbiten,[2] Randall E. Youngman,[2] John C. Mauro,[3] Ashutosh Goel[1,*]

[1] Department of Materials Science and Engineering, Rutgers, The State University of New Jersey, Piscataway, NJ 08854-8065, United States

[2] Science and Technology Division, Corning Incorporated, Corning, NY 14831, United States

[3] Department of Materials Science and Engineering, The Pennsylvania State University, University Park, PA 16802, United States of America

[*] Corresponding author
Email: ag1179@soe.rutgers.edu; Ph: +1-848-445-4512

Abstract

The uncontrolled growth of nepheline ($NaAlSiO_4$) crystals during the manufacturing of sodium aluminosilicate glasses via the fusion draw or float techniques and during the vitrification of some of the sodium- and alumina-rich nuclear waste glasses is a well-known problem. The addition of B_2O_3 to suppress the crystallization in these glasses is well documented in the literature. Other advantages of B_2O_3 is that it lowers the viscosity of the glass melt and, if incorporated in its trigonal coordination state, will improve the intrinsic damage resistance of the final glass product. Hence, B_2O_3 has been an integral component of glass compositions for advanced industrial applications and for nuclear waste vitrification. However, one major disadvantage of adding B_2O_3 to alkali aluminosilicate based glasses is its adverse impact on their chemical durability due to the rapid hydrolysis of $B^{[3,4]}$–O–$B^{[3,4]}$ bonds in comparison to (Si, Al)–O–(Si, Al) bonds. Therefore, designing a boron-containing alkali aluminosilicate based functional glass with minimal tendency towards crystallization and high chemical durability requires an in-depth fundamental understanding of the mechanism through which B_2O_3 tends to suppress crystallization in these glasses. There is no current consensus on the fundamental mechanism through which B_2O_3 tends to suppress nepheline crystallization in these glasses. Based on the mechanisms described and the questions raised in the preceding literature, the present study focuses on addressing the ongoing debate through a detailed structural and thermo-kinetic investigation of glasses designed in the Na_2O–Al_2O_3–B_2O_3–SiO_2 based quaternary system over a broad composition space. Using a combination of Raman and (1D and 2D) nuclear magnetic resonance spectroscopies along with equilibrium and non-equilibrium viscosity, and liquidus temperature measurements, it has been shown that the substitution of Si–O–Al by Si–O–B linkages in the glass structure results in a significant increase in the glass forming ability as well as an increase in the liquidus viscosity (slower diffusivity), thereby suppressing the nepheline crystallization.

1. Introduction

Nepheline ($Na_6K_2Al_8Si_8O_{32}$) is a rock-forming tectosilicate mineral which has been studied by geologists for more than a century.[1] In the field of materials science, nepheline based glass-ceramics gained attention during the 1960s when a tableware based upon glazed nepheline-based glass-ceramic formulation was commercially sold by Corning Glass Works under the brand-name Centura®.[2] Since then, nepheline based glass-ceramics have been explored for several technological applications including dental materials,[3, 4] microwave compatible glass-ceramics (due to their low absorption of microwave energy),[5, 6] and transparent and opaque glass-ceramics for electronic packaging (owing to their ability to be chemically strengthened by ion-exchange).[7, 8] While a controlled crystal growth is desirable in the abovementioned technological applications, there are other applications where nepheline crystallization is undesirable. For example, the crystallization of nepheline during the cooling of some of the sodium and alumina-rich `waste glass (in steel canisters) at Hanford Site in Washington state is considered to be detrimental for the long-term performance (chemical durability) of the vitrified waste form.[9, 10, 11] Similarly, nepheline crystallization is a problem during the manufacturing of alkali aluminosilicate based glasses by fusion draw technique[12] aimed for their application as display glass in consumer electronics, for example, mobile phones, computers, and other displays.[12, 13, 14, 15]

One long-known solution to suppress nepheline crystallization in glass melts is the addition of B_2O_3 to the batch.[16, 17, 18] The added advantage of B_2O_3 is that it lowers the viscosity of the glass melt as well as improves the intrinsic damage resistance of the glass by reducing its Young's and shear modulus (when present in three-fold coordination).[19, 20] Due to these reasons, B_2O_3 has been

an integral component of glass compositions either intended for forming by fusion draw or nuclear waste vitrification. On the other hand, one major disadvantage of adding B_2O_3 to alkali aluminosilicate based glasses is its adverse impact on their chemical durability due to the rapid hydrolysis of $B^{[3,4]}$–O–$B^{[3,4]}$ bonds in comparison to (Si, Al)–O–(Si, Al) bonds.[21, 22, 23] Therefore, designing a boron-containing alkali aluminosilicate based functional glass with minimal tendency towards crystallization and high chemical durability requires an in-depth fundamental understanding of the mechanism through which B_2O_3 tends to suppress crystallization in these glasses. The literature on this topic reveals an ongoing debate with various researchers presenting diverging viewpoints. According to Marcial et al.,[24] it is the coordination number of alkali cations in the sodium aluminoborosilicate glass that controls the propensity of nepheline crystallization. While the coordination number (CN) of sodium in carnegieite (an orthorhombic polymorph of nepheline) crystal is 6, according to the researchers, an increase in B/Al ratio in glasses in the system $NaAl_{(1-x)}B_xSiO_4$ results in an increase in its CN from 6 to 6.4, thus resulting in the suppression of crystallization.[24] However, the validity of this hypothesis needs to be verified over a broader composition space. According to Li et al.,[16] B^{3+} effectively competes with Al^{3+} for Na^+ as charge compensation of BO_4^- units, thus reducing the activity or concentration of $[AlO_{4/2}]^-$–Na^+ resulting in suppression of nepheline crystallization. Further, according to a recent study by Lee and Lee,[20] there exists a non-negligible concentration of Al–O–Al linkages in the glass with composition 25 Na_2O – 25 Al_2O_3 – 50 SiO_2 (mol.%) resulting in imperfect aluminum avoidance. An increase in Al/B ratio leads to a decrease in Al–O–Al and Si–O–Al linkages and an increase in the proportion of Si–O–B linkages in the glasses. Although not mentioned by Lee and Lee,[20] connecting their results about the structure of $NaAl_{(1-x)}B_xSiO_4$ glasses with the crystallization behavior of the same series of glasses reported by Marcial et al.,[24] another possible explanation for

suppressed crystallization may be an increased thermal stability (due to reduction in Al–O–Al and an increase in Si–O–B linkages) with increasing B/Al ratio. These diverging schools of thought do not allow for development of a holistic understanding of the fundamental mechanism through which B_2O_3 tends to suppress nepheline crystallization.

In the present study, an attempt has been made to address this debate and present a mechanism for suppression of nepheline crystallization (as a function of B_2O_3) based on the structure and kinetics of crystallization in sodium aluminoborosilicate glasses. Accordingly, glasses with varying Al_2O_3/B_2O_3 and SiO_2/B_2O_3 ratios have been designed in the quaternary system Na_2O–Al_2O_3–B_2O_3–SiO_2 in the primary crystallization field of nepheline ($NaAlSiO_4$) and its polymorphs. The concentration of B_2O_3 in both series of glasses has been varied between 0 – 20 mol.% at an increment of 5 mol.% to compare the impact of changing Al_2O_3/B_2O_3 ratio with SiO_2/B_2O_3 ratio on the structure, viscosity, and crystallization tendency of the glasses. Raman and magic angle spinning – nuclear magnetic resonance (MAS NMR) spectroscopies have been used to study the structure of glasses and partitioning of boron in resultant glass-ceramics. Further, from the standpoint of classical nucleation and crystal growth theory, nucleation and crystal growth rates are governed by overall diffusivities of constituent atoms,[25, 26] which are further dependent on the viscosity and temperature as per the Stokes-Einstein (SE) equation. It is therefore anticipated that probing the viscosity at the liquidus temperatures of the aluminoborosilicate glasses and melts under investigation will aid in developing an understanding of the role of boron in the suppression of nepheline crystallization. Therefore, a combination of isothermal and non-isothermal crystallization studies in conjunction with beam-bending and rotational viscometer and liquidus temperature measurements have been utilized to understand the structural and thermodynamic drivers controlling the nepheline crystallization in sodium boroaluminosilicate glasses.

2.1 Glass synthesis

Glasses with varying B_2O_3/SiO_2 (labeled as SB–*x*) and B_2O_3/Al_2O_3 ratios (labeled as BA–*x*), where *x* represents the batched B_2O_3 content in mol.%, were synthesized using the melt-quench technique. The boron-free baseline glass is designated as BL, which represents the stoichiometric nepheline ($Na_2O•Al_2O_3•2SiO_2$) composition. Homogeneous mixtures of batches (corresponding to 70 g oxide glass), comprising SiO_2 (Alfa Aesar; >99.5%), Na_2SiO_3 (Alfa Aesar; anhydrous, tech.), Al_2O_3 (ACROS Organics; extra pure; 99%) and H_3BO_3 (ACROS Organics; extra pure, 99+%) were melted in 90%Pt–10%Rh crucibles in an electric furnace at temperatures varying from 1450-1650 °C for 2 h. The melts were quenched on a copper plate followed by annealing for 1 h and then slowly cooling to room temperature. The annealing temperatures were determined from the estimated values of glass transition temperature (T_g) using the SciGlass database, as T_g – 50 °C. The amorphous nature of the samples was confirmed by using X-ray diffraction (XRD; PANalytical – X'Pert Pro; Cu K_α radiation; 2θ range: 10º–90º; step size: 0.013º s^{-1}). The experimental composition of glasses was analyzed by inductively coupled plasma – optical emission spectroscopy (ICP-OES; PerkinElmer Optima 7300 V) and flame emission spectroscopy (for sodium; PerkinElmer Flame Emission Analyst 200). Table 1 presents the batched and experimental compositions of the studied glasses.

2.2 Thermal characterization of glasses

2.2.1 Differential Scanning Calorimetry

The glasses were crushed to produce coarse glass grains in the particle size range of 0.85 to 1 mm. Differential scanning calorimetry (DSC) data were collected using a Simultaneous Thermal Analyzer (NETZSCH 449 F5 Jupiter, Burlington, MA) in the temperature range of 30 ºC – 1600

ºC at a heating rate (β) of 10 °C min^{-1} under a constant flow of nitrogen gas. The temperatures, corresponding to the onset of glass transition (T_g), onset (T_c), and peak (T_p) of crystallization and melting (T_m), were obtained from DSC scans. The DSC data reported for any glass composition are the average of at least three thermal scans.

2.2.2 Viscosity measurements

An Orton RSV-1700 rotating spindle viscometer equipment (Westerville, OH) comprising a Brookfield HB-DV2T viscometer head fitted with a platinum spindle was used to measure the viscosity of five glasses, i.e., BL, SB-10, SB-20, BA-10, and BA-20, upon cooling from the melt stage. The high-temperature calibration of the viscometer as well as the establishment of the spindle measurement constant[27] over the temperature range of interest were performed using the National Institute of Standards and Technology (NIST) 710 soda-lime silica standard reference glass.[28] Approximately 400 grams of glass frit was placed inside a 200 mL 90%Pt-10%Rh crucible. The crucible was then loaded in the viscometer furnace set at a temperature varying between 1000 – 1500 °C depending on the B_2O_3 content in the glass and heated for ~ 10 hours to remove bubbles and to ensure a homogenous melt while avoiding volatilization of components. The melt was then further heated to its maximum temperature and held for ~30 minutes to ensure that the temperature reached steady state. The rotating platinum spindle was lowered into the melt and rotated at a speed varying between 1 rpm to 80 rpm, where the speed was reduced as the viscosity increased. The viscosity measurements were made by gradually decreasing the temperature of the melt until the spindle torque became too high to prevent it from rotating in the melt. At any given temperature, once the viscosity value stabilized (as a function of time), it was recorded along with the temperature readings using the Molten Glass and Molten Ash Viscometer software provided by Orton Ceramics.

Three-point equilibrium beam-bending method[29] was utilized to measure the viscosity of glasses near the glass transition temperature, T_g. Each reported data point corresponds to a viscosity measurement after an isothermal hold. At each temperature, viscosity was observed during the isothermal hold until the viscosity reached a plateau as a function of time. Therefore, these viscosity values correspond to the thermodynamic equilibrium state independent of thermal history, and they are only a function of the glass/melt composition.

2.2.3 Liquidus temperature measurements

Liquidus temperature (T_L) measurements were performed on five glass compositions, namely, BL, SB-10, SB-20, BA-10, and BA-20, by following ASTM C829 – 81 standard using gradient furnace method. Accordingly, the samples were crushed in a metallic pestle-mortar to obtain ~35 grams of powdered glass in a particle size range of 300 to 425 μm. The powders were washed using ethanol, followed by acetone, and dried overnight in an oven at 100 °C. The dried powdered samples were placed in Pt-Rh boats (15 cm x 0.5 cm base; 0.6 cm height; 16.2 cm x 0.8 cm top) and inserted in the muffle tube of the gradient furnace. Using calorimetric data obtained from DSC, a tentative range of liquidus temperature was determined by locating the end of the melting curve of each composition. Accordingly, the gradient furnace (Orton GTF – 1616STD – G) was heated to a temperature so that the glass at the hot-end of the platinum boat was completely melted, while the remaining part of the boat fall in the expected range of liquidus temperature. The platinum boat was allowed to heat inside the furnace for a duration varying between 1 – 7 days depending on the crystallization tendency of the glass. After the completion of the heating cycle, the boat was removed from the furnace and allowed to cool on a steel plate. After confirming the amorphous nature of the hot-end and the crystalline nature of cold-end by XRD, the sample was observed under an optical microscope (moving from the hot-end to cold-end) to determine the point where

the first crystal in the melt was formed. By measuring the length of this point from the hot-end and correlating that value with the temperature vs. length curve of the gradient furnace, the liquidus temperature (T_L) of the sample was determined. Further, XRD (PANalytical – X'Pert Pro; Cu $K_{\alpha 1}$ radiation) was used to determine the identity of the crystalline phase.

2.2.4 Crystalline phase evolution in glasses

To understand the non-isothermal crystalline phase evolution in glasses as a function of their composition, glass pieces (~2-3 gram) were heated (in Al_2O_3 crucibles) to different temperatures (Carbolite BLF 1800 furnace) in the crystallization region (per DSC data) at 10 °C min^{-1} and were air quenched as soon as the desired temperatures were reached. All the heat-treated samples were characterized qualitatively by powder XRD (PANalytical – X'Pert Pro; Cu $K_{\alpha 1}$ radiation).

The crystalline phase evolution in the glasses under isothermal conditions was studied by heating the glasses at 950 °C for 24 hours (β = 10°C min^{-1}) in a muffle furnace (Thermo Fisher Scientific; Thermolyne F47925-80) in ambient atmosphere. The heat-treated glass samples were allowed to cool to room temperature in the furnace. The resulting glass-ceramics were divided into two parts. The first part of the sample was crushed to powder with particle size < 45 μm and mixed with 10 wt.% Al_2O_3 as an internal standard for quantitative crystalline phase analysis by XRD using the Rietveld analysis method (JADE). The crystalline phase evolution data for qualitative analysis was obtained using the XRD parameters described in section 2.1. The data for quantitative phase analysis was obtained using PANalytical X'Pert Pro XRD with a Cu-K_α tube, 45 kV, and 40 mA, in the 2θ range of 10 – 90° with 0.006565° 2θ step size, and dwell time of 23.97 s.

2.3 Structural characterization of glasses

2.3.1 Raman spectroscopy

Raman spectra of glasses were obtained using a Renishaw inVia Raman spectrometer equipped confocal microscope system using a 532 nm wavelength laser, operating at 500 mW power. Unpolarized Raman spectra were acquired in the range of 100 to 1700 cm^{-1} wavenumbers on pieces of glasses focused at a 20× magnification. Ten accumulations were taken for each scan with a spectral resolution of 1 cm^{-1}, with an exposure time of 10 s cm^{-1}. All of the recorded spectra were subjected to baseline correction followed by intensity normalization by dividing the values on the y-axis by the maximum value on the y-axis.

2.3.2 Nuclear magnetic resonance (NMR) spectroscopy

The structure of selected glasses and glass-ceramics has been studied using multi-nuclear magic-angle spinning (MAS) and multiple quantum magic angle spinning (MQMAS) NMR spectroscopy. The MAS NMR spectra of ^{11}B and ^{23}Na were acquired using commercial spectrometers (DD2, Agilent) and MAS NMR probes (Agilent). The samples were powdered in an agate mortar, packed into 3.2 mm zirconia rotors, and spun at 20 kHz for ^{11}B MAS NMR and 22 kHz for ^{23}Na MAS NMR. ^{23}Na MAS NMR data was collected at 16.4 T (185.10 MHz resonance frequency), using a 0.6 μs (~π/12 tip angle) pulse width for uniform excitation of the resonances. A range of 400–1000 acquisitions were co-added, and the recycle delay between scans was 2 s. ^{11}B MAS NMR experiments were conducted at 16.4 T (224.52 MHz resonance frequency), incorporating a 4 s recycle delay, short rf pulses (0.6 μs) corresponding to a π/12 tip angle, and signal averaging of 400 to 1000 scans. The acquired spectra were processed with minimal apodization and referenced to aqueous boric acid (19.6 ppm) and aqueous NaCl (0 ppm). Fitting of the MAS NMR spectra was performed using DMFit[30] and, accounting for distributions in the quadrupolar coupling constant, the CzSimple model was utilized for ^{23}Na MAS NMR spectra. The ‘‘Q MAS ½” and Gaus/Lor functions were used to fit 3- and 4-fold coordinated boron resonances

in the ^{11}B MAS NMR data, respectively, and N_4 was calculated from the relative areas of these peaks, with a small correction due to the overlapping satellite transition of the 4-fold coordinated boron peak.[31]

2D 3QMAS NMR experiments were conducted at 16. 4 T (185.1 MHz resonance frequency) using an Agilent DD2 spectrometer and 3.2 mm MAS NMR probe. Samples were packed into 3.2 mm zirconia rotors and spun at 22 kHz. These data were collected using the hypercomplex shifted-echo pulse sequence.[32] For ^{23}Na 3QMAS NMR, RF pulses were calibrated to provide optimized signal-to-noise ratios, typically resulting in hard pulse widths of 5.1 and 1.8 μs, and a soft z-filter reading pulse of 20 μs. 24 to 240 acquisitions were collected for each of 32 to 128 t_1 points, with an isotropic sweep width of 100 kHz and a recycle delay of 2 to 5 s. All 3QMAS NMR data were processed (shear transformed and shift referenced) using commercial software and without any added line broadening in either dimension. Projections onto the MAS and isotropic shift axes were done by summing the maximum signal to give a skyline-type projection.

3. Results

3.1 Compositional analysis of glasses

All the glasses synthesized in this study appeared transparent and proved to be non-crystalline via XRD, as shown in Figure S1. The compositional analysis of these glasses has been conducted using ICP-OES and flame emission (for sodium oxide) spectroscopy. The concentration of Na_2O has been observed to be 0 – 3% less than the batched Na_2O weight fraction, while the amount of B_2O_3 has been observed to be 0 – 6% less than its batched weight fraction (Table 1). The wt.% of SiO_2 content is also observed to be 0 – 5% less than its batched weight fraction. These losses can be attributed to the volatility of Na_2O and B_2O_3 arising from the relatively high melting temperatures of these glass batches (1450 °C and above). Nevertheless, these deviations are

unlikely to impact the trends in the compositional dependence of the properties presented in this study.

3.2 Structure of glasses

3.2.1 Raman spectroscopy

The normalized and baseline-corrected Raman spectra of glasses belonging to SB-series and BA-series have been presented in Figures 1(a) and 1(b), respectively. For the convenience of the readers, we have divided the Raman spectra of the studied glasses into the following four regions: **Region I:** 250 cm^{-1} – 650 cm^{-1}; **Region II:** 650 – 850 cm^{-1}; **Region III:** 850 – 1250 cm^{-1}, and **Region IV:** 1250 – 1600 cm^{-1} and the assignments of all Raman bands have been summarized in Table 2. In the low-frequency Region I, the Raman spectrum of the baseline glass (BL) shows bands centered at ~448, 490 and 560 cm^{-1}. These bands have been reported to be related to the 442, 492, and 604 cm^{-1} bands in pure SiO_2 glass, respectively, and have been attributed to the mixed stretching-bending vibrational modes of T-O-T (T = Si, Al) in six-membered, four-membered and three-membered T-O-T rings respectively.[33, 34, 35, 36] The band observed at 490 cm^{-1}, known as the D1 band, indicates the presence of four-membered rings;[37, 38] while the band at 448 cm^{-1} in BL glass has a tail to lower frequency probably related to five- or six-membered ring sizes.[36] As B_2O_3 is substituted for SiO_2 (SB-series), the intensity of the 560 cm^{-1} band decreases, which is attributed to the so-called D2 bands representing breathing vibrations of three-membered rings with one or more Al atoms.[37, 38, 39] The three bands in Region I tend to merge with increasing B_2O_3 content, resulting in a broad band from 300 to 620 cm^{-1} in glass SB-20. The merging of bands may be attributed to the broader distributions of bond angles and bond distances arising in the glass network that comprises aluminate and silicate tetrahedra along with trigonal borate entities. Similar

trends are, however, not observed when B_2O_3 is substituted for Al_2O_3 (BA-series). With increasing B_2O_3 substitution for Al_2O_3 to 15 mol.% and above (BA-15 and BA-20), a new band at 630 cm^{-1} can be observed. This band has been attributed to breathing mode in danburite-like borosilicate rings or formation of metaborate rings.[21, 40, 41] Danburite is a mineral of composition $CaO{\cdot}B_2O_3{\cdot}2SiO_2$ where boron exists as BO_4^- tetrahedra, charge compensated by Ca^{2+}. Manara et al.[42] have argued that the 630 cm^{-1} band can also be attributed to a similar structure with Na^+ instead of Ca^{2+}, thus making the formula of borosilicate rings as $Na_2O{\cdot}B_2O_3{\cdot}2SiO_2$. Interestingly, this band is not observed when B_2O_3 is substituted for SiO_2, since in SB-series Na/Al = 1, in an ideal case scenario, it is expected that all the Na^+ will be consumed in charge compensating the AlO_4^- tetrahedra. Therefore, boron in the SB series of glasses is expected to be three-coordinated. On the other hand, in BA-series, substitution of B_2O_3 for Al_2O_3 results in a per-alkaline composition. Therefore, an increasing number of Na^+ cations are available to charge-compensate BO_4^- units. This explains the reason for the absence of the 630 cm^{-1} band corresponding to danburite-like rings from the Raman spectra of the SB glass series. The results are in good agreement with the findings of Lee and Lee,[20] where they reported an increase in Si–O–B linkages upon increasing B/Al ratio in the $NaAl_{(1-x)}B_xSiO_4$ glass system. Further, according to Marcial et al.,[24] an increase in B_2O_3 concentration in $NaAl_{(1-x)}B_xSiO_4$ should result in the formation of "reedmergnerite – like" rings, B[xSi, (4-x)Al], rather than "danburite-like" rings. The characteristic Raman band for reedmergnerite rings is at ~586 cm^{-1}.[40, 42] While the BA-series glasses show a band at 570 cm^{-1} which has been attributed to vibrations of three-membered aluminosilicate rings with one or more Al atoms, a distinct band at 586 cm^{-1} has not been observed. Therefore, the presence of "reedmergnerite–like" rings, while possible, could not be confirmed in the present study.

In Region II between 650 to 850 cm^{-1}, the subtle changes occurring due to the changing B_2O_3/SiO_2 (SB-series) and B_2O_3/Al_2O_3 (BA-series) ratios are more complicated to decipher due to the overlapping of bands corresponding to different structural moieties. As seen in Figure 1, all SB-series and BA-series glasses, along with BL, show a broad band in this region. The literature suggests that the band between 700 to 800 cm^{-1} peaking at 740 cm^{-1} in the BL glass can be attributed to T-O-T (T= Si, Al) bending modes or motion of Si atom in its oxygen cage or to T–O stretching vibrations involving oxygen motions in the T-O-T plane.[33, 34, 43] The contributions from these vibrations are most likely present in both SB- and BA-series of glasses as well. Furthermore, according to the literature on Raman spectroscopy of borosilicate glasses, a band in the region 720–730 cm^{-1} could be assigned to chain-type meta-borate groups containing non-bridging oxygens (NBOs).[44] Similarly, it has been reported in the literature that a band at 770 cm^{-1} in borosilicate glasses is generally attributed to the symmetric breathing vibration of six-membered rings containing BO_4 tetrahedra.[41, 42, 45] However, as will be shown in the next section, the glasses in the SB-series are devoid of any NBOs with all boron present in trigonal form; while glasses in the BA-series do contain NBOs along with a significant fraction of tetrahedral boron. Therefore, the possibility of a contribution from bands corresponding to meta-borate units and breathing vibrations of rings containing BO_4 tetrahedra can be negated in case of SB-series glasses, while the contributions from such vibrations are possible in BA-series of glasses. As mentioned earlier, these results are in good agreement with the ^{17}O MAS NMR results reported on $NaAl_{(1-x)}B_xSiO_4$ glasses by Lee and Lee.[20] Furthermore, a very low-intensity band can be observed at ~830 cm^{-1} in SB-10, SB-15, and SB-20 glasses which is likely associated with borate groups containing trigonal boron, possibly structures similar to boroxol rings.[46] Such a band has not been observed in BA-series glasses.

The Region III between 850 and 1250 cm^{-1} shows a prominent high-intensity band in the spectra of all the samples. Generally, this region shows bands corresponding to asymmetric and symmetric Si–O vibrations in fully polymerized tetrahedral units.[33, 35, 40, 42, 47] Since the baseline glass (BL) corresponding to stoichiometric composition of nepheline ($NaAlSiO_4$) is fully polymerized, the bands primarily consist of (Si, Al)–O stretching modes in $Si(OAl)_x$ species – where x is the number of AlO_4 tetrahedra attached to the SiO_4 tetrahedron. McMillan et al.[33] have suggested that the bands at 1120, 1000, and 935 cm^{-1} in nepheline glass are indicative of Si(OAl), $Si(OAl)_2$, and $Si(OAl)_3$ units respectively.[33, 48] With the substitution of B_2O_3 for SiO_2 (SB-series), there is an overall decrease in the intensity of this broad band, which is due to the decreasing SiO_2 content, but there is no significant change in its peak position. On the other hand, when B_2O_3 is substituted in place of Al_2O_3 (BA-series), there is an increase in the intensity of this broad band along with a shift in the peak position to a higher wavenumber from 1000 cm^{-1} in BL to 1060 cm^{-1} in BA-20. Furthermore, with increasing B_2O_3 content in BA-series, the shape of the band changes, as it becomes narrower and develops a tail on the lower wavenumber side. These changes in the shape of the band can be attributed to an increase in Si–O–B linkages, an increasing proportion of $Si–O^-$ stretching vibrations in tetrahedra containing NBOs (Q^3 units), and the reducing number of Si–O–Al linkages.[40, 41, 49]

The Region IV between 1250 cm^{-1} and 1600 cm^{-1} generally shows bands corresponding to B-O stretching vibrations in chain-type metaborate groups.[21, 40, 41, 42, 45] With increasing B_2O_3 substitution against SiO_2 (SB-series), two low-intensity bands are observed at 1290 and 1420 cm^{-1} in the case of SB-15 and SB-20 which can be attributed to B–O stretching vibrations involving oxygen connected to different groups and ring vibrations respectively.[50] On the other hand, when B_2O_3 is substituted against Al_2O_3 (BA-series), a band appears at 1460 cm^{-1}, which has also been

previously reported in the Raman spectra of similar glass compositions.[21] The band has been attributed to BØO$^-$ triangles (Ø = bridging oxygen, O$^-$ = NBO) connected to other BO_3 units based on the literature from alkali borate and alkali aluminoborate glasses.[40, 41] Thus, as discussed above, the presence of chain-type meta-borate units with NBOs is highly likely in the BA-series of glasses, while it is unlikely in SB-series glasses due to the absence of NBOs. Here it should be noted that according to Lee and Lee,[20] the NBOs in the glass system $NaAl_{(1-x)}B_xSiO_4$ are created only in the silicate network. However, the presence of a Raman band at ~1460 cm^{-1}, corresponding to BØO$^-$ triangles, points towards the presence of NBOs in both silicate and borate network in the glass structure. Therefore, further structural investigations in this glass system are warranted.

3.2.2 MAS NMR spectroscopy

Figure 2 presents the ^{23}Na MAS NMR spectra of selected glasses from the SB- and BA-series. All spectra show a broad featureless peak, which is characteristic of amorphous materials, with a maximum close to -10 ppm. The spectrum of glass BL is consistent with our previous work[51, 52, 53] and other reports on sodium aluminosilicate glasses which denote this frequency to Na^+ acting as a charge compensating cation and not creating any NBOs.[54, 55, 56] As evident from Figure 2, the range of chemical shifts is relatively small in both SB- and BA-series, which, coupled with a large quadrupolar interaction for ^{23}Na, requires the use of two-dimensional MQMAS NMR experiments to determine the chemical shifts and quadrupolar product with greater accuracy.

The ^{23}Na MQMAS NMR spectra of select SB- and BA-series glasses have been presented in Figure 3. The ^{23}Na MQMAS NMR spectrum of all glasses shows a dominant chemical shift distribution along with broadening induced by quadrupolar coupling which confirms a wide distribution of Na^+ environments which is characteristic for glasses. The isotropic chemical shift (δ_{CS}) and quadrupolar coupling constant (C_Q) values for the spectra presented in this study have

been computed by fitting the MAS NMR spectra using DMFit. Although fitting of ^{23}Na MAS NMR data does provide these key parameters, the lineshapes for ^{23}Na in amorphous solids make reliable determination of C_Q rather difficult, so instead, we have utilized ^{23}Na MQMAS NMR data to better estimate the average quadrupolar coupling parameters in these glasses. The frequencies corresponding to the MAS projection (δ_{MAS}) as well as the isotropic projection (δ_{iso}) have been used to calculate the isotropic chemical shifts (δ_{CS}) and quadrupolar coupling products (P_Q) by using equations (1) and (2) respectively:[32]

$$\delta_{CS} = \frac{10}{27}(\delta_{MAS}) + \frac{17}{27}(\delta_{iso}) \qquad (1)$$

$$P_Q = (\delta_{iso} - \delta_{MAS})^{1/2} \times 5.122 \times 0.1851018 \qquad (2),$$

where the latter two constants (5.122 and 0.1851018) are determined by the nuclear spin of ^{23}Na (I=3/2) and the Larmor frequency used for these ^{23}Na MQMAS NMR experiments, respectively. P_Q is related to the quadrupolar coupling constant, C_Q, as $P_Q = C_Q(1+\eta^2/3)^{1/2}$, where η is the asymmetry of the quadrupolar coupling interaction. The δ_{CS} and P_Q values obtained for the aforementioned glasses have been presented in Table S3. With increasing B_2O_3 substitution against SiO_2 (SB-series), the δ_{CS} values do not show a significant trend in variation, as the values range from -4.1 ppm in BL to -4.4 ppm in SB-10 and -4.2 ppm in SB-20. This suggests that there is no significant change in the Na-O bond length or coordination number when B_2O_3 is replaced against SiO_2. There is a slight decrease in the quadrupolar coupling product from 1.75 MHz in glass BL to 1.53 MHz in glass SB-20 (as shown in Table S3).

On the other hand, with increasing B_2O_3 substitution against Al_2O_3 (BA-series), there is a positive shift in δ_{CS} from -4.1 ppm in BL to -3.5 ppm in BA-20, suggesting a decrease in Na-O bond length or coordination number,[54] along with an increase in the quadrupolar coupling constant from 1.75 MHz in glass BL to 1.9 MHz in BA-20 (Table S3). Previous studies have shown that a

sodium ion in position as a charge compensator exhibits a larger Na-O bond length than in position as a modifier.[57, 58] With the substitution of B_2O_3 for Al_2O_3, there is a change in the role of Na^+ ions from being solely a charge compensator in the boron-free glass (BL), to both a charge compensator and network modifier in boron-containing glasses, which explains the decrease in the average Na-O bond distance. This change in the role of Na^+ ions is also reflected by the increase in P_Q values with increasing B_2O_3.

Further, the chemical shift in the ^{23}Na MQMAS NMR spectra of glasses has been interpreted using the empirical correlation derived by Koller et al.[59] for crystalline sodium silicates described in Equation 3.

$$\delta_{CS} = -133A + 107 \qquad (3)$$

where,

$$A = \sum_i W_i / r_i^3 \qquad (4)$$

Here, W_i is the valence of the i_{th} oxygen, which can be computed from the empirical parameters in Ref.,[60] and r_i is the distance to that oxygen. The typical valence is $W = 2$ for oxygen (both bridging and non-bridging) as has been proposed by Zwanziger et al.[61], while the Na–O distance (r_i) has been calculated using Equation 5 proposed by Lee and Stebbins for sodium aluminosilicate glasses.[54]

$$\delta_{CS} = -64.4 \times d(Na-O) + 168.3 \qquad (5)$$

According to Zwanziger et al.,[61] these estimates can be used to derive the average CN (n) for sodium in the glass by performing the sum in Equation 4 over the n nearest neighbors and using W and r as described in Equation 6.

$$A \approx n\left(W / r^3\right) \qquad (6)$$

Table 3 presents the values of δ_{CS}, Na–O bond length (r), A, and average CN of sodium (n). The average CN of sodium in the baseline sodium aluminosilicate glass has been estimated to be 8.01. There is no significant trend in change in CN when B_2O_3 is substituted in place of SiO_2, as the CN increases to 8.08 in SB-10 and then reduces to 8.03 in SB-20, which fall within the margin of error. On the other hand, there is a slight decreasing trend in CN when B_2O_3 is substituted against Al_2O_3, as the CN value drops from 8.01 in the BL glass to 7.95 in BA-10 and 7.89 in BA-20. It is generally assumed that δ_{CS} values obtained from fitting have an uncertainty of ±1 ppm, which amounts to an uncertainty of ~0.22 in the estimation of CN. This suggests that a small amount of measurement or fitting error does not account for a large change in CN. To the best of author's knowledge, there does not exist any literature reporting the values of sodium CN in sodium aluminoborosilicate glasses except for Marcial et al.[24] where they have reported an increase in the CN of sodium in $NaAl_{(1-x)}B_xSiO_4$ based glasses from 6 to 6.4. The estimated value of sodium CN for nepheline glass in the present study is in good agreement that reported by Lee and Stebbins.[62] However, the estimated sodium CN is comparatively higher than that calculated by McKeown et al.[63] or Neuville et al.[64] from the Na K-edge XANES of nepheline glass (CN ≈ 5). As is evident, there does not exist an agreement on the exact coordination environment of non-framework cations in alkali aluminosilicate glasses in the literature. According to Lee and Stebbins,[54] the noticeable discrepancy in sodium CN values calculated from ^{23}Na MAS NMR spectra and Na K-edge XANES may be due to the processes associated with phase shift corrections in EXAFS or the fact that ^{23}Na chemical shift is rather insensitive to CN, with significant overlap between CN values of 5 and 6.[59] Therefore, a more detailed look at the effect of the oxygen–bonding environment around Na is needed.

Figure 4 presents the ^{11}B MAS NMR spectra of glasses from SB (Figure 4a) and BA-series (Figure 4b). The broad peak between 10 ppm and 20 ppm corresponds to trigonal boron (BO_3), while the peak appearing near 0 ppm corresponds to tetrahedral boron (BO_4). Table 4 presents the quantification of boron units in glasses as determined from ^{11}B MAS NMR spectra. In the glasses with varying B_2O_3/SiO_2 ratio, boron primarily exists in trigonal coordination (BO_3) owing to the unavailability of sodium ions to convert BO_3 to BO_4 units (as shown in the ^{27}Al MAS NMR spectra provided in Figure S4, aluminum is present solely in tetrahedral coordination in both SB- and BA-series glasses). The consumption of all the sodium cations to charge-compensate AlO_4^- units also rules out the possible existence of NBOs in the glasses from SB-series.

In the case of glasses with varying B_2O_3/Al_2O_3 ratio, the ^{11}B MAS NMR signal shows a combination of trigonal and tetrahedral boron with an increasing proportion of BO_4^- units with increasing B_2O_3 content. Since B_2O_3 is being substituted at the expense of Al_2O_3, and not all the excess $Na^{+\dagger}$ is used to convert BO_3 to BO_4^- units, a fraction of sodium cations will act as network modifiers, thus creating NBOs in the borosilicate glass network, corroborating the results of Raman spectroscopy. The trend is generally consistent with those reported for ^{11}B MAS NMR studies on the same glass compositions.[20, 21, 24] Table 4 presents the number of NBOs per tetrahedron (NBO/T) being produced in the structure of glasses from BA-series as calculated using boron speciation data from ^{11}B MAS NMR spectroscopy. As is evident from Table 4, the NBO/T fraction increases with increasing B/Al ratio in the investigated glasses.

3.3 Glass transition and viscosity behavior of glasses and melts

† Excess $Na^+ = [Na^+]_{total} - [Na^+]_{AlO4}$, i.e., sodium cations left after charge compensating AlO_4^- units.

Figures S2(a) and S2(b) present the DSC scans of all the glasses in the SB and BA-series, respectively, while Table 5 summarizes different transformation temperatures obtained from these scans. The glass transition temperatures (T_g^{DSC}) of the studied glasses were obtained from the onset of the endothermic peak in the glass transition range. Furthermore, the viscosity data measured using the beam-bending method has been used to obtain the glass transition temperature corresponding to a viscosity of 10^{12} Pa s, which has been designated as T_g^{vis} and presented in Table 5. As evident, the T_g^{DSC} and T_g^{vis} are in good agreement with each other. The T_g^{DSC} value of the baseline glass (BL) was found to be the highest among all the investigated glasses and was observed to decrease with increasing B_2O_3/SiO_2 (SB- series) and B_2O_3/Al_2O_3 (BA- series) ratios. Although the T_g^{DSC} decreases with increasing B_2O_3 content, the trends in the variation in T_g^{DSC} of the two series of glasses are significantly different, as shown in Figure S3. In the SB series, an increasing B_2O_3 concentration results in a slightly non-linear decrease in the T_g^{DSC}. This trend can be explained on the basis of decreasing network connectivity in the glass structure as tetrahedral SiO_4 units are replaced by less-constrained BO_3 units that reduce the overall rigidity of the glass network. However, since B_2O_3 is replaced against SiO_2 on a molar oxide basis, removal of every SiO_4 tetrahedron is accompanied by addition of 2 BO_3 trigonal species in the network. The resulting non-linear variations of both SiO_4 and BO_3 species as a function of B/Si ratio may help in explaining the reducing magnitude of decrease in T_g with increasing B_2O_3.

In the glasses in BA-series, substituting 10 mol.% B_2O_3 for Al_2O_3 results in a sharp decrease in the T_g^{DSC} value from 802 °C (BL glass) to 538 °C (BA-10). This may be attributed to a sudden drop in the fraction of Al–O–Al linkages from ~30% to nearly zero, as has been shown by Lee and Lee.[20] The presence of Al–O–Al linkages in the glass structure usually result in higher T_g values in the alkali and alkaline-earth aluminosilicate and aluminoborate glasses.[53, 65, 66] Further increase

in B_2O_3 concentration has a relatively smaller impact on the T_g^{DSC} values of the resulting glasses (Figure S3) which may be explained on the basis of two competing mechanisms in the glass structure – (1) an increase in the BO_4 fraction (over BO_3) resulting in higher network connectivity, and (2) gradual replacement of stronger Si–O–Al linkages by weaker Si–O–B linkages[20, 23] along with an increasing NBO fraction leading to a weaker network.

The experimental high-temperature viscosity values of glass melts in the range of 10^1 to 10^3 Pa s (from rotation viscometry), and the near-T_g viscosity values of glasses (from equilibrium beam bending viscometry) have been presented in Table S1. In order to cross-check the viscosity values measured in the present investigation, the viscosity values of baseline glass (BL) were compared with those reported in the literature for similar glass compositions, as presented in Table S2. Toplis et al.[67] reported viscosity values of two melts with their chemical composition close to $NaAlSiO_4$, where the glass with Na/(Na + Al) = 51 was labeled as NAS50:51, while the one with Na/(Na+Al) = 49 was labeled as NAS50:49. The viscosity values of the BL glass melt obtained in our study are in good agreement with those reported by Toplis et al.,[67] while the near-T_g viscosity of BL glass is in good agreement with that reported by Le Losq et al.[39] The substitution of B_2O_3 for SiO_2 (SB-series) or Al_2O_3 (BA-series) leads to a decrease in the viscosity, which is expected, but the extent of the impact varies significantly depending on whether B_2O_3 has been substituted for Al_2O_3 or SiO_2.

The viscosity values obtained using the beam-bending method have been used to calculate the kinetic fragility, m, of the glass melts as described in Equation 5.[68]

$$m = \frac{d\,(log_{10}\eta)}{d(\frac{T_g}{T})} \qquad (5)$$

$at\ T = T_g^{vis}$, where the T_g^{vis} corresponds to the temperature at which equilibrium viscosity is 10^{12} Pa s. The melts closer to Arrhenian behavior are defined as strong and have a low fragility value, while the melts having a large departure from Arrhenian behavior have higher fragility values and are defined as fragile.[68, 69] Figure 5 presents the viscosity of glasses collected using the beam-bending method in the near-T_g regime as a function of T_g/T (also known as Angell plot),[69] and the fragility values calculated using Eqn. (5). The *m* of the baseline glass (BL) obtained by this method is in good agreement with that presented by Toplis et al.[67] An increase in B_2O_3/SiO_2 ratio in the glass melts (SB series) leads to a decrease in fragility from 38.7 in BL to 33.5 in SB-10, while further increase leads to an increase in fragility to 36.6. Overall, the substitution of B_2O_3 in place of SiO_2 exhibits a minimal impact on their fragility values with an average value is 36 ± 3 along the whole series of glasses. On the other hand, an increase in the B_2O_3/Al_2O_3 ratio (BA series) in glasses results in a significant increase in the fragility of glass melts with the value of *m* increasing from 38.7 (for BL) to 57.3 (for BA-20).

When correlating the atomic structure of glasses with their fragility, it can be observed that the trends observed in fragility are directly proportional to their NBO/T concentration, as shown in Figure 6. Similar correlations between the structure and kinetic fragility index of sodium aluminoborosilicate glasses have also been reported by Zheng et al.[70] where they have attempted to explain these trends on the basis of changes in boron coordination and temperature-dependent topological constraint theory.[71] However, the glass structure vs. fragility trends observed in the present study, as well as those reported by Zheng et al.,[70] have also been widely reported in boron-free glasses in the literature.[67, 72, 73] In terms of glass structure, the kinetic fragility has been shown to depend on the network connectivity in the glass. A higher fragility is directly proportional to a

greater loss in the configurational entropy upon the cooling of a melt. A lowering of network connectivity due to an increase in NBO concentration, thus, results in a higher fragility index.[72]

3.4 Crystallization behavior of glasses

3.4.1 Crystallization behavior as predicted from DSC analysis

The DSC scans of the investigated glasses (as shown in Figure S2a and Figure S2b, and data presented in Table 4) reveal interesting information about their crystallization behavior. The BL glass shows an onset of crystallization at 924 °C, and a crystallization peak at 961 °C, followed by melting at 1526 °C, although the thermal analysis data of this glass in our previous studies did not show any crystallization curve.[51] This may be due to the difference in the thermal history of glass particles. While the BL glass in our previous study was obtained by water-quenching of the melt,[51] in the present study it has been obtained by pouring the melt on a steel plate followed by annealing.

The substitution of 5 mol.% B_2O_3 for SiO_2 results in a drop in the crystallization onset temperature and appearance of two exothermic peaks followed by a lowered melting temperature (compared to glass BL). Further increase in the B_2O_3 content to 10 mol.% leads to the formation of a peak with a shoulder. The appearance of two exothermic crystallization curves in the DSC scans of glasses SB-5 and SB-10 indicates either the formation of two or more crystalline phases or polymorphic transformations in a crystalline phase as a function of temperature. With further increase in B_2O_3 content to ≥15 mol.%, only one crystallization peak is observed, and the T_c, T_p, and T_m values continue to drop. The difference in T_c and T_g ($\Delta T = T_c - T_g$), which is indicative of the glass' resistance towards devitrification, has been calculated and presented in Table 5. While the ΔT value for BL glass is estimated to be 122 °C, the substitution of 5 mol.% B_2O_3 for SiO_2

reduces it to 106 °C denoting an increase in the tendency towards crystallization. However, a further increase in B_2O_3 content >5 mol.% results in a gradual rise in the ΔT values from 106 °C (for glass SB-5) to 232 °C (for glass SB-20).

Among the BA-glass series, only BA-5 and BA-10 glasses show crystallization peaks followed by subsequent melting curves for the as-formed crystal phases. The crystallization temperatures are significantly lower for the glasses in BA-series as compared to their counterparts in the SB-series with the same B_2O_3 content. A drop in ΔT is observed from 122 °C (in BL) to 112 °C in BA-5. However, further increase in B_2O_3 content to 10 mol.% results in a substantial increase in ΔT to 151 °C, denoting suppression in crystallization tendency. Since the glasses with B_2O_3>10 mol.% in BA-series do not exhibit any crystallization peaks, ΔT cannot be calculated for these glasses.

3.4.2 Non-isothermal heat treatment of glasses

The evolution of crystalline phases in glasses has been observed by heat-treating glass samples at different temperatures, followed by air quenching. Heat treatment schedules have been designed to traverse various crystallization regions of interest, as obtained from DSC. Figure 7 presents the powder X-ray diffraction patterns of glasses heated at different crystallization temperatures and air quenched. The first traces of crystallinity in the baseline glass BL are observed (in XRD) at 960 °C with the formation of low-carnegieite ($NaAlSiO_4$; orthorhombic; PDF#98-007-3511) as shown in Figure 7a. At higher temperatures (1120 °C), the SiO_2-rich nepheline phase ($Na_{7.15}Al_{7.2}Si_{8.8}O_{32}$; hexagonal; PDF#97-006-5960) starts to crystallize in the sample co-existing with the low-carnegieite, as shown in Figure 7b. Upon replacing SiO_2 with B_2O_3, as in glass SB-5 and SB-10, the crystallization still initiates at 960 °C with the formation of low-carnegieite (Figure 7a), followed by the formation of Si-rich nepheline from 1080 °C (not shown). Upon further

increase in the B_2O_3 content (for SiO_2) in SB-15 and SB-20 glasses, crystallization is found to initiate with the formation of nepheline. Interestingly, the Bragg peaks matching to both stoichiometric nepheline ($NaAlSiO_4$; PDF#97-008-5553; hexagonal) and SiO_2-rich nepheline ($Na_{7.15}Al_{7.2}Si_{8.8}O_{32}$; hexagonal; PDF#97-006-5960) are detected in heat-treated glasses SB-15 and SB-20. The glasses SB-15 and SB-20 were observed to melt at temperatures above 1120 °C.

In the BA-glass series, substituting 5 mol.% B_2O_3 for Al_2O_3 (BA-5) results in complete suppression of low-carnegieite as SiO_2-rich nepheline has been observed to crystallize as the first phase at 840 °C, shown in Figure 7c. Further increase in the temperature results in an increase in the crystallinity in the sample, as is evident from the high-intensity XRD peaks in Figure 7d. However, the crystalline phase assemblage remains unaffected. The glasses with $B_2O_3 \geq 10$ mol.% show no signs of crystallinity (in XRD) during non-isothermal heat treatments, as is evident from Figures 7c and 7d, which is in agreement with the DSC results.

3.4.3 Isothermal heat treatment of glasses

Isothermal heat treatments on glasses in the SB-series have been conducted at 950 °C for 24 h, while the glasses in BA-series have been subjected to heat-treatment at 850 °C for 24 h. The lower isothermal heat-treatment temperature for glasses in BA-series has been chosen because glasses BA-15 and BA-20 showed melting above 850 °C during non-isothermal heat treatments. Figure 8 presents the results of the qualitative and quantitative phase analysis of the isothermally heat-treated samples as obtained by Rietveld refinement on the XRD data. The baseline glass BL, when heated at 950 °C for 24 h, forms a glass-ceramic which comprises mainly of low-carnegieite (~48 wt.%), nepheline (~ 9.9 wt.%) and minor amounts of low- quartz (SiO_2; hexagonal; PDF# 97-004-1474). The substitution of 5 mol.% B_2O_3 for SiO_2 (SB-5) results in two changes in the phase assemblage – (1) complete suppression of low-carnegieite, and (2) decrease in the

amorphous character from 34.5 wt.% in BL to 22.1 wt.% in SB-5 (in agreement with ΔT trends observed from DSC data). Upon further increase in substitution of B_2O_3 for SiO_2 from 5 mol.% to 20 mol.%, there is a gradual increase in the amorphous content from 26% to 70%, with nepheline being the dominant phase in all the glass-ceramics (~28% in SB-20). Similar to the non-isothermal heat-treatment results, two types of nepheline are detected in SB-series glass-ceramics, namely, stoichiometric nepheline ($NaAlSiO_4$; PDF#97-008-5553; hexagonal) and SiO_2-rich nepheline ($Na_{7.15}Al_{7.2}Si_{8.8}O_{32}$; hexagonal; PDF#97-006-5960) as is evident from Figure S5.

In the case of isothermal heat treatments of glasses from BA-series, the BL glass-ceramic is found to contain higher amorphous content (38.5 wt.%) than when it was heated at 950 °C, which is not surprising, given the lower heat-treatment temperature. The low-carnegieite phase is found to be 19.6 wt.%, while SiO_2-rich nepheline ($Na_{7.15}Al_{7.2}Si_{8.8}O_{32}$; hexagonal; PDF#97-006-5960) is found to be 11.9 wt.%. As B_2O_3 is substituted for Al_2O_3, there is a dramatic decrease in the amorphous content such that the BA-5 glass-ceramic is mainly with the SiO_2-rich nepheline phase (80.7 wt.%) while the low-carnegieite content reduces to zero. With an increase in B_2O_3-content to 10 mol.%, as in BA-10, there is again an increase in amorphous content to 70.6 wt.% while SiO_2-rich nepheline is the only crystalline phase detected. Upon further increase to 15 and 20 mol.% of B_2O_3, crystallinity is completely suppressed.

3.5 Liquidus temperature

The liquidus temperatures obtained from the gradient furnace method are presented in Table 5. The liquidus temperature (T_L) of BL ($NaAlSiO_4$) glass is measured as 1534 °C, which is in good agreement with the literature.[49] Since B_2O_3 is a low melting oxide, substitution of B_2O_3 for Al_2O_3 or SiO_2 results in a decrease in the T_L of glasses. However, the degree of reduction in the liquidus

temperature is much higher when B_2O_3 is substituted for Al_2O_3 in comparison to its substitution for SiO_2 on an equimolar basis, as shown in Table 6. We have not been able to measure the T_L of glass BA-20 even after 7 days of experimentation due to its high resistance towards devitrification. Thermochemical modeling of sodium aluminoborosilicates has predicted the T_L of glass $NaBSiO_4$ to be ~1000 K (726.85 °C).[74] Since BA-20 composition has the formula $NaAl_{0.2}B_{0.8}SiO_4$, its T_L is likely to be closer but higher than that of $NaBSiO_4$. Furthermore, the liquidus viscosity was estimated by interpolating the viscosity values at liquidus temperatures. For accurate prediction of viscosity, we have used the Mauro-Yue-Ellison-Gupta-Allan (MYEGA) model.[75] The MYEGA equation (equation 6) includes the following three parameters: glass transition temperature- T_g, fragility index- m, and the infinite temperature limit of liquid viscosity, η_∞.

$$log_{10}\eta(T) = log_{10}\eta_\infty + (12 - log_{10}\eta_\infty)\frac{T_g}{T}\exp\left[\left(\frac{m}{12 - log_{10}\eta_\infty} - 1\right)\left(\frac{T_g}{T} - 1\right)\right] \quad (6)$$

Using a Levenberg Marquardt iteration logarithm in the Origin® Graphing and Analysis software, we have successfully fit the data. Thus, the liquidus viscosity has been estimated and presented in Table 6. Figure 9 presents an illustration of the methodology used to estimate the liquidus viscosity for glass BA-10. The liquidus viscosity increases with increasing B_2O_3 content in glasses. However, when comparing the impact of substitution of an equimolar concentration of B_2O_3 (10 mol.%) in the BL glass for SiO_2 vs. Al_2O_3, the glass BA-10 has a significantly higher liquidus viscosity than the glass SB-10.

Figure 10 presents the X-ray diffractograms of the samples obtained after liquidus temperature measurements. As is evident from Figure 10 and Table 6, non-stoichiometric cubic carnegieite ($Na_{1.15}Al_{1.15}Si_{0.85}O_4$; cubic; #PDF97-028-0474) was the phase that crystallized in the glasses BL and SB-10 at T_L. The crystallization of cubic carnegieite in BL glass at T_L is not surprising as it is

the high-temperature polymorph of nepheline and is known to crystallize as the first phase during slow-cooling of glass melt with stoichiometric nepheline composition.[51, 76] Further, the formation of cubic carnegieite in the glass SB-10 may be attributed to the glass being SiO_2-deficient. According to Withers et al.,[77] although cubic carnegieite is a superstructure of β-cristobalite (the high-temperature stable polymorph of silica), its tetrahedral framework is more aluminate than silicate, which is why it forms in systems that are SiO_2-deficient. However, the intriguing part is the formation of SiO_2–rich nepheline ($Na_{7.15}Al_{7.2}Si_{8.8}O_{32}$; hexagonal; PDF#97-006-5960) in glasses SB-20 and BA-10 at T_L, thus suppressing the formation of cubic-carnegieite. This is likely because the T_L of both the glasses is much lower than the temperatures at which cubic-carnegieite is stable (>1200 °C).

3.6 Structural characterization of isothermally heat-treated glasses by MAS NMR

3.6.1 ^{23}Na MAS and MQMAS NMR

^{23}Na MAS NMR and MAS projections of MQMAS NMR data for the isothermally heat-treated glasses are provided in Figure 11. The 2D MQMAS NMR plots have been presented in Figure S6 of the supplementary data. As is evident, the ^{23}Na MAS NMR projections from MQMAS NMR data of the glass-ceramics contain more resolved features (compared to the MAS NMR spectra and due to the manner in which the projections are generated) thus, providing more qualitative insight into the different Na environments. The ^{23}Na MAS NMR spectra of BL glass-ceramic heat-treated at 950 ºC for 24h are shown in Figure 11a. The signal has a much narrower width compared to its glassy analog (Figure 2), a typical characteristic of a highly crystalline sample. The peaks for ^{23}Na MAS NMR spectra belonging to nepheline crystal usually lie within the region -5 to -20 ppm,[78, 79, 80, 81] while for low-carnegieite, the ^{23}Na spectra has been reported to lie within -10 ppm

to +6 ppm,[51, 80] ranging in value due to the magnetic field dependence of the MAS NMR experiment. The ^{23}Na MAS NMR spectrum of BL glass-ceramic heat-treated at 950 ºC for 24 h (Figures 11a and 11b) shows a peak at 2.3 ppm which has an isotropic chemical shift value of 5.4 ppm likely corresponding to carnegieite, while it shows shoulders in the negative ppm range, extending up to -10 ppm, as well as a low-intensity shoulder near +11 ppm. Since the BL glass-ceramic is dominated by the carnegieite phase, the nepheline peaks are likely contained within the up-field shoulder. Our previous studies have reported similar results, but with slight differences in peak positions.[51, 52]

In the case of SB-10 and SB-20 glass-ceramics, the MAS projections (Figure 11b) of their ^{23}Na MQMAS NMR spectra show a combination of several sharp peaks within broad signals, indicative of multiple crystalline phases and a higher amorphous fraction in these samples. The δ_{CS} values of crystalline peaks (Table S4) indicate that multiple crystalline phases exist. The sites with a δ_{CS} value around -2.0 ± 1 ppm in SB-10 and SB-20 glass-ceramics can be assigned to the oval site in the nepheline crystal structure, whereas the sites at lower frequencies with δ_{CS} values near -12 ppm can be assigned to the larger hexagonal site. As discussed in the section 3.4.3, two types of nepheline phases have been observed in the SB-glass-ceramics – first, a stoichiometric $NaAlSiO_4$, and second, a SiO_2-rich nepheline ($Na_{7.2}Al_{7.2}Si_{8.8}O_{32}$), which explains the multiple peaks observed in the spectra of SB-10 and SB-20 glass-ceramics. Furthermore, the overall shapes of the MAS projections of MQMAS NMR spectra of SB-10 and SB-20 show resemblance to some studies reported in the literature, for example, Stebbins et al.[79] have shown changes in the ^{23}Na MAS NMR spectra of synthetic nepheline minerals heat-treated at higher temperatures due to Na^+ occupying larger sites rapidly exchanging with those occupying smaller sites. It is likely that a similar type of exchange of Na^+ ions between different sites (oval and hexagonal) may have taken place as a

result of heat-treatments of SB-series glass-ceramics. It is difficult to comment on whether the shifts in peaks corresponding to nepheline can be attributed to a decrease in Na-O bond length since these peaks contain contributions from amorphous as well as crystalline components, which can complicate the signal and lead to shifts in peak position of the crystalline peak alone.

The ^{23}Na MAS NMR spectra and MAS projections of MQMAS NMR of isothermally heat-treated glasses from BA-series are shown in Figures 11(c) and 11(d) respectively. The detailed δ_{CS} and P_Q values obtained from peak positions in the MQMAS NMR spectra, using equations (1) and (2), have been presented in the Table S4. The δ_{CS} of the residual glass in BL glass-ceramic heat-treated at 850 ºC has been calculated to be -3.7 ppm, along with a P_Q value of 1.70 MHz. The δ_{CS} values of the most dominant peak is 5.7 ppm, which is consistent with the ^{23}Na signal in carnegieite crystal.[51] The δ_{CS} value of the second most dominant sharp peak is -2.2 ppm which most likely corresponds to nepheline. In the case of BA-10 glass-ceramic, the two dominant crystalline signals have δ_{CS} values of -5.4 ppm and -19.2 ppm that are consistent with the signals for nepheline,[51, 79, 81] whereas the residual glass has a δ_{CS} value of -3.3 ppm. Comparing the δ_{CS} values of original glasses (Table 3) along with those of the residual glassy phase in the corresponding glass-ceramics, it can be observed that the formation of crystals leads to a reduction in the δ_{CS} value of residual glass – indicating a decrease in the Na-O bond length or coordination number. This can also indicate an increase in the proportion of Na^+ ions acting as network modifiers since the formation of an aluminosilicate crystal such as nepheline makes the residual glassy network rich in boron. The lack of any crystalline signal in the ^{23}Na NMR spectra of BA-20 sample heated at 850 ºC is not surprising since the sample remained amorphous as shown by the XRD results. There is no change in the δ_{CS} value as compared to the glass counterpart (-3.5 ppm), though, a change in P_Q value is observed.

3.6.2 ^{11}B MAS NMR

The ^{11}B MAS NMR spectra of glass-ceramics obtained from isothermal heat treatments have been presented in Figure 12. While the ^{11}B MAS NMR spectra of SB-10 and SB-20 glasses show all of the boron in trigonal coordination, the ^{11}B MAS NMR spectra of glass-ceramics of SB-10 and SB-20 reveal the presence of ~4% BO_4^- units in both the samples. Additionally, the broadness of the peaks depicts the amorphous nature of boron present in the glass-ceramics. This indicates that: (i) all the boron stays in the residual glassy phase, not entering the crystal structure of nepheline, and (ii) considering that the Na/Al = 1 in the parent glass composition, the resultant glass-ceramic has a per-alkaline (Na/Al>1) residual glassy phase as is evident from the formation of BO_4 units. Correspondingly, the nepheline phase detected in the glass-ceramics is non-stoichiometric, as the quantitative phase analysis via XRD shows the presence of Si-rich nepheline ($Na_{7.15}Al_{7.2}Si_{8.8}O_{32}$; hexagonal; PDF#97-006-5960). As the chemical formula of Si-rich nepheline suggests, this phase is slightly more Na-deficient than Al-deficient, which suggests that there are likely some Na^+ ions in excess of the AlO_4^- units in the residual glassy phase, thus resulting in the conversion of BO_3 to BO_4^-.

In the case of heat-treated samples from the BA series, the BA-10 glass-ceramic shows an increase in the proportion of BO_4^- from 32.5% in glass to 43.3%, similar to what has been observed in the SB- glass-ceramics. Apart from that, a sharp peak is observed which denotes a small fraction (~1.4%) of BO_4 units in a crystalline environment. It should be noted that this peak was not observed in the ^{11}B MAS-NMR spectra of glass-ceramics in the SB series. According to the existing literature, boron does not enter the nepheline crystal structure.[82, 83] However, considering that no boron-related crystalline phases have been observed in the XRD or SEM-EDS (not shown), the assignment of this peak is difficult to ascertain. It is possible that a small concentration of BO_4

units may substitute for AlO_4 units in the nepheline crystal structure. However, further studies are needed to validate this assertion. Further increase in B_2O_3 to 20 mol.% results in very little change in the NMR spectra of heat-treated glass (compared to glass) as the fraction of BO_4^- units reduce from 60.9 % to 57.8 %. Since BA-20 glass did not show any crystallization upon isothermal heat treatment, the change in boron coordination may be attributed to the impact of thermal history, as has been shown in the literature.[84, 85, 86]

4. Discussion

4.1 Correlation between structure and crystallization behavior of glasses

As mentioned in the introduction, according to Li et al.,[16] B^{3+} effectively competes with Al^{3+} for preferential charge compensation of BO_4^- units in sodium aluminoborosilicate glasses, thus reducing the activity or concentration of $[AlO_{4/2}]^-$–Na^+ resulting in suppression of nepheline crystallization. However, this does not seem to be the case for glasses with Na/Al = 1, and all the boron tends to stay in three-coordination (SB-series). This shows that B^{3+} does not effectively compete with Al^{3+} for preferential charge compensation of BO_4^- units. Further, according to Marcial et al.,[24] as B/Al ratio increases in the $NaAl_{(1-x)}B_xSiO_4$ glass system, the average CN of sodium increases from 6.0 to 6.4. Since the average coordination numbers of sodium in carnegieite and nepheline are ~6 and ~8, respectively,[87, 88] an increase in coordination number of sodium from 6.0 to 6.4 has been proposed as a possible explanation for the formation of nepheline over carnegieite with an increase in B_2O_3 concentration. Further, it has been suggested that since the average sodium coordination number in the glasses does not reach close to ~8 to allow for significant crystallization of nepheline, the crystallization is frustrated with increasing B_2O_3 content in glasses.[24] Since the CN (Na) calculations in the present study do not concur with those

calculated by Marcial et al.[24] (as has been discussed in section 3.2.2) it is difficult to compare the results from the two studies.

In our opinion, it is the replacement of Si–O–Al linkages by $Si^{[4]}$–O–$B^{[3,4]}$ linkages in the glasses with varying B/Al ratio that tend to suppress the nepheline crystallization. Our opinion is based on the formation of danburite – like rings in the BA-series of glasses with B_2O_3 > 10 mol.%. Interestingly, nepheline crystallization is completely suppressed in glasses BA-15 and BA-20, i.e. glasses with the formation of danburite rings in the glass structure. On the other hand, in glasses with varying B_2O_3/SiO_2 ratio, $Si^{[4]}$–O–$Al^{[4]}$ linkages seem to dominate over $Si^{[4]}$–O–$B^{[3,4]}$ linkages as (i) the concentration of Al_2O_3 in these glasses remains constant, (ii) the majority of Al stays in four-coordination being charge compensated by sodium, (iii) the Raman peak corresponding to danburite – like rings is absent, and (iv) B–O–Al linkages are not expected with increasing B_2O_3 concentration as has been shown by Lee and Lee.[20] The presence of Si–O–Al linkages in the glass where Na/Al ratio lies in the crystallization field of nepheline or its polymorphs, provides a pathway for the crystallization of these phases. Also, the impact of reducing Al–O–Al linkages on the suppression of crystallization cannot be negated.[20] However, detailed structural characterization (for example, ^{27}Al 3Q MAS-NMR and ^{17}O MAS-NMR) needs to be performed on glasses in SB-series to ascertain the presence/absence of these structural units.

4.2 Influence of B_2O_3 on viscous flow dynamics in sodium aluminoborosilicates

In the present study, we have measured the viscosity of melts in the high-temperature range using rotational viscometry as well as near-T_g viscosities using the beam-bending method. The variation in viscosity with changing composition can be related to structural properties of the melt using the Adam-Gibbs theory as described in Equation 7.[89]

$$log_{10}\eta(T) = A_e + B_e/TS_c(T) \qquad (7)$$

where A_e is the infinite temperature viscosity limit,[75] $\log_{10}\eta_\infty$; $S_c(T)$, the configurational entropy of the melt, is a function of temperature; and B_e is a proportionality constant considered analogous to the activation energy in an Arrhenian model of viscous flow. Therefore, B_e/S_c at temperature T can be calculated as described in Equation 8.

$$\frac{B_e}{S_c(T)} = (log_{10}\eta(T) - A_e)T \qquad (8)$$

Adam and Gibbs showed that for $T = T_g$, the ratio $B_e/S_c(T_g)$ is be given by Equation 9.[89, 90]

$$\frac{B_e}{S_c(T_g)} = z^*(T_g)\Delta\mu/k \qquad (9)$$

where z^* is the size of the smallest rearrangement units, $\Delta\mu$ is the potential barrier to structural rearrangement, and k is the Boltzmann constant. While B_e and S_c both cannot be calculated with the experiments conducted in the present study, their ratio can be calculated from the viscosity data. Further, according to Toplis et al.,[90] $\Delta\mu$ plays a more dominant role in controlling $B_e/S_c(T_g)$ than z^*, and that $\Delta\mu$ is controlled by the microscopic mechanisms responsible for viscous flow, denoting the significance of $B_e/S_c(T_g)$. Since viscosity at $T_g = 10^{12}$ Pa s, we can calculate the value for $\frac{B_e}{S_c(T_g)}$ using Equation 10.

$$\frac{B_e}{S_c(T_g)} = (12 - log_{10}\eta_\infty)T_g \qquad (10)$$

The values of B_e/S_c at T_g in the present study decreases as B_2O_3 is substituted for SiO_2 or Al_2O_3, as summarized in Table 6. Furthermore, it has been reported in the literature that among B_e and S_c, the latter shows a more dominant change, while B_e has an insignificant change with composition.[90, 91, 92] Therefore, it is reasonable to assume that a decrease in B_e/S_c implies an increase in S_c value at T_g with increasing B_2O_3. This can be correlated well with the changing local atomic structure of the glasses. According to Toplis et al.[90], the potential barrier for viscous flow

is higher in the case of SiO_2 as compared to fully polymerized $NaAlSiO_4$ because the Si–O–Si bond is stronger than Si–O–Al bond. The inclusion of B_2O_3 introduces Si–O–B bonds in the network, which are weaker than Si–O–Si and Si–O–Al bonds. This results in a further decrease in the potential barrier for viscous flow. The drop in B_e/S_c at T_g, which implies an increase in S_c at T_g, is more significant when B_2O_3 is substituted for Al_2O_3 (BA-series) because of the decreasing network connectivity and introduction of NBOs – which do not exist in SB-series.

4.3 Correlating viscosity with crystallization

It is generally assumed that the kinetics of crystallization in glasses, i.e., crystal growth rates, are governed by diffusivity (D).[25] Since diffusivity and crystal growth rates are difficult to measure, it is desirable to obtain their correlation with measurable properties, for example viscosity. The Stokes-Einstein (SE) equation (Equation 11) is commonly used to describe the relation between viscosity (η) and diffusivity (D).

$$D = \frac{RT}{N_A}\frac{1}{6\pi\eta a} \qquad (11)$$

where N_A is Avogadro's number, R is gas constant, T is temperature, and a is the size of the particle. This relation has been reported to be valid only at high temperatures near melting.[26, 93] At a lower temperature, known as decoupling temperature, T_d (where $T_d = 1.15 - 1.25*T_g$),[93] the decoupling of diffusion and viscosity occurs. Above T_d, the SE equation is supposed to be valid, and the replacement of the diffusion coefficient with viscosity is expected to work well in the description of crystal growth kinetics near the melting temperatures.[26, 93, 94, 95] Table 8 presents the estimated T_d range for the glasses investigated in this study. Since the T_L of all the glasses in this study are higher than their respective T_d range, it is safe to assume that the SE equation (Equation 11) is valid at liquidus temperature. Therefore, we have used this temperature (as an example) for

understanding the impact of B_2O_3 on the crystal growth rates in the present study. Thus, substituting $\eta = \eta(T_L)$ in equation 11, it is evident that the higher the liquidus viscosity, $\eta(T_L)$, the lower the diffusivity (D). Further, it has been shown that due to decoupling of viscosity and diffusion, the crystal growth rate, u_{kin}, relates with viscosity as described in Equation 12.[95, ‡]

$$u_{kin} \propto \eta^{-\xi} \text{ since } (u_{kin} \propto D) \qquad (12)$$

where the exponent ξ expresses the extent of decoupling of viscosity from diffusion. Therefore, D is directly proportional to the crystal growth rate, u_{kin}. In the abovementioned context, it is evident that an increase in the viscosity of melts above T_d when B_2O_3 is a substitute for SiO_2 or Al_2O_3 results in lower diffusivity resulting in reduced crystal growth rate. Since the $\eta(T_L)$ is considerably higher in glasses when B_2O_3 is substituted for Al_2O_3 (compared to its substitution for SiO_2), as shown in Table 6, the glasses in BA-series exhibit stronger suppression of crystallization.

Recently, Jiusti et al.[96] derived a parameter for glass-forming ability (GFA), which utilizes the liquidus temperature (T_L) and viscosity at the liquidus ($\eta(T_L)$), demonstrating that GFA $\propto$ $[\eta(T_L)/T_L^2]$. Using the results of liquidus temperature and liquidus viscosity values in the present study, we have calculated the $[\eta(T_L)/T_L^2]$ values for the glasses investigated in the present study, as presented in Table 8. The GFA increases with increasing B_2O_3 content in the studied glasses. However, the value of GFA for glass increases ~3× when 10 mol.% B_2O_3 is substituted for SiO_2 in glass SB-10 (compared to glass BL) whereas it increases by ~31× when an equal concentration of B_2O_3 is substituted for Al_2O_3 in the glass BA-10 (compared to glass BL). Our results from isothermal heat-treatments corroborate this prediction, as we observe a suppression in crystallization with increase in boron-content, which is more significant when B_2O_3 is substituted

‡ Ediger et al.[95] have further mentioned that ξ is inversely correlated with fragility, but because of the phenomenon of decoupling, fragility cannot be directly correlated to crystallization.

against Al_2O_3; and they add further experimental validity to the parameter for glass-forming ability put forth by Jiusti et al.[96]

5. Conclusions

The present study aims at understanding the structural and thermo-kinetic drivers resulting in the suppression of crystallization of nepheline–like phases in sodium aluminosilicate glasses as a function of B_2O_3. Two sets of glasses, the first with varying B_2O_3/SiO_2 ratio and the second with varying B_2O_3/Al_2O_3 ratio, have been studied for their structure, crystallization behavior, viscosity and liquidus temperature. It has been found that while B_2O_3 tends to suppress nepheline crystallization, varying B_2O_3/Al_2O_3 ratio has a more significant impact when compared to the B_2O_3/SiO_2 ratio. When B_2O_3 is substituted against SiO_2, Si–O–Al linkages dominate over Si–O–B linkages, which provide a pathway for crystallization of nepheline in SB-series of glasses. On the other hand, when B_2O_3 is substituted against Al_2O_3, the replacement of Si–O–Al linkages with Si–O–B linkages suppresses nepheline crystallization. These inferences can also be correlated to a more significant increase in the liquidus viscosity (decreased diffusivity) when B_2O_3 is substituted for Al_2O_3 instead of SiO_2, thus resulting in suppressed crystallization. Furthermore, the substitution of B_2O_3 in place of Al_2O_3 leads to the formation of NBOs. This leads to a decreased network connectivity in the glass structure, thus, resulting in an increase in the fragility index and also implying an increase in the configurational entropy at T_g.

Acknowledgment

This work was supported by funding provided by the Department of Energy (DOE), Office of River Protection, Waste Treatment & Immobilization Plant (WTP), through contract numbers DE-EM0003207 and 89304018CEM000006.

References

1. N. L. Bowen, *Am. J. Sci.*, 1912, **33**, 551-573.
2. W. Holand and G. H. Beall, *Glass-Ceramic Technology*, John Wiley & Sons, Inc., Hoboken, NJ, 2012.
3. M. C. Wang, N. C. Wu and M. H. Hon, *Mater. Chem. Phys.*, 1994, **37**, 370-375.
4. E. M. A. Hamzawy and E. A. M. El-Meliegy, *Mater. Chem. Phys.*, 2008, **112**, 432-435.
5. J. F. MacDowell, *Am. Ceram. Soc. Bull.*, 1984, **63**, 282.
6. J. F. MacDowell, US Pat., US4341872A, 1982.
7. A. J. Ellison,A. L. Moore and T. L. Werner, US Pat., 20150284288, 2015.
8. G. H. Beall, C. M. Smith, S. A. Tietjie, US Pat., 2018105453A1, 2018.
9. J. D. Vienna, J. O. Kroll, P. R. Hrma, J. B. Lang and J. V. Crum, *Int. J. Appl. Glass Sci.*, 2017, **8**, 143-157.
10. J. S. McCloy, M. J. Schweiger, C. P. Rodriguez and J. D. Vienna, *Int. J. Appl. Glass Sci.*, 2011, **2**, 201-214.
11. A. Goel, J. S. McCloy, R. Pokorny and A. A. Kruger, *J. Non-Cryst. Solids: X*, 2019, **4**, 100033.
12. M. J. Dejneka, A. J. Ellison, and J. C. Mauro, US Pat., 20180050952A1, 2018.
13. T. M. Gross, X. Guo, and C. M. Smith, US Pat., 20190077696A1, 2019.
14. A. J. Ellison, J. C. Mauro, D. M. Noni, L. M. Thirion, and N. Venkataraman, US Pat., 20150140299A1, 2015.
15. J. C. Mauro, US Pat., 9764981B2, 2014.
16. H. Li, P. Hrma, J. D. Vienna, M. Qian, Y. Su and D. E. Smith, *J. Non-Cryst. Solids*, 2003, **331**, 202-216.
17. H. Li, J. D. Vienna, P. Hrma, D. E. Smith and M. J. Schweiger, in *Symposium on Scientific Basis for Nuclear Waste Management XX Vol. 465*, eds. W. J. Gray. and I. R. Triay. Materials Research Society Conference Proceedings, Boston, MA, 1996, pp. 261-268.
18. K. M. Fox, T. B. Edwards and D. K. Peeler, *Int. J. Appl. Ceram. Tech.*, 2008, **5**, 666-673.
19. D. B. Dingwell, R. Knoche, S. L. Webb and M. Pichavant, *Am. Mineral.*, 1992, **77**, 457-461.
20. A. C. Lee and S. K. Lee, *Geochim. Cosmochim. Acta*, 2020, **268**, 325-347.
21. E. M. Pierce, L. R. Reed, W. J. Shaw, B. P. McGrail, J. P. Icenhower, C. F. Windisch, E. A. Cordova and J. Broady, *Geochim. Cosmochim. Acta*, 2010, **74**, 2634-2654.
22. N. Stone-Weiss, R. E. Youngman, R. Thorpe, N. J. Smith, E. M. Pierce and A. Goel, *Submitted*, 2019.
23. S. K. Lee, C. B. Musgrave, P. Zhao and J. F. Stebbins, *J. Phys. Chem. B*, 2001, **105**, 12583-12595.
24. J. Marcial, M. Saleh, D. Watson, S. W. Martin, C. L. Crawford and J. S. McCloy, *J. Non-Cryst. Solids*, 2019, **506**, 58-67.
25. J. W. P. Schmelzer, *J. Non-Cryst. Solids*, 2008, **354**, 269-278.

26. J. W. P. Schmelzer, A. S. Abyzov, V. M. Fokin, C. Schick and E. D. Zanotto, *J. Non-Cryst. Solids*, 2015, **429**, 45-53.
27. V. L. Wiesner, U. K. Vempati and N. P. Bansal, *Scr. Mater.*, 2016, **124**, 189-192.
28. A. Napolitano and E. G. Hawkins, *J. Res. Nat. Bur. Stand. A*, 1964, **68**, 439-448.
29. O. Gulbiten, J. C. Mauro, X. Guo and O. N. Boratav, *J. Am. Ceram. Soc.*, 2018, **101**, 5-11.
30. D. Massiot, F. Fayon, M. Capron, I. King, S. Le Calvé, B. Alonso, J. O. Durand, B. Bujoli, Z. Gan and G. Hoatson, *Magn. Reson. Chem.*, 2002, **40**, 70-76.
31. D. Massiot, C. Bessada, J. Coutures and F. Taulelle, *J. Magn. Reson.*, 1990, **90**, 231-242.
32. J. P. Amoureux, C. Fernandez, and S. Steuernagel, *J. Magn. Reson. A, 1996,* **123**, 116-118.
33. P. McMillan, B. Piriou and A. Navrotsky, *Geochim. Cosmochim. Acta*, 1982, **46**, 2021-2037.
34. P. McMillan, *Am. Mineral.*, 1984, **69**, 622-644.
35. A. N. Novikov, D. Neuville, L. Hennet, Y. Gueguen, D. Thiaudière, T. Charpentier and P. Florian, *Chem. Geol.*, 2017, **461**, 115-127.
36. S. K. Sharma, J. F. Mammone and M. F. Nicol, *Nature*, 1981, **292**, 140-141.
37. C. L. Losq, D. R. Neuville, P. Florian, G. S. Henderson and D. Massiot, *Geochim. Cosmochim. Acta*, 2014, **126**, 495-517.
38. F. L. Galeener, *Solid State Commun.*, 1982, **44**, 1037-1040.
39. C. Le Losq, D. R. Neuville, W. Chen, P. Florian, D. Massiot, Z. Zhou and G. N. Greaves, *Sci. Rep.*, 2017, **7**, 16490.
40. D. Manara, A. Grandjean and D. R. Neuville, *J. Non-Cryst. Solids*, 2009, **355**, 2528-2531.
41. M. Lenoir, A. Grandjean, Y. Linard, B. Cochain and D. R. Neuville, *Chem. Geol.*, 2008, **256**, 316-325.
42. D. Manara, A. Grandjean and D. Neuville, *Am. Mineral.*, 2009, **94**, 777-784.
43. F. A. Seifert, B. O. Mysen and D. Virgo, *Am. Mineral.*, 1982, **67**, 696-717.
44. A. K. Yadav and P. Singh, *RSC Advances*, 2015, **5**, 67583-67609.
45. A. Winterstein-Beckmann, D. Moencke, D. Palles, E. I. Kamitsos and L. Wondraczek, *J. Non-Cryst. Solids*, 2014, **401**, 110-114.
46. B. N. Meera and J. Ramakrishna, *J. Non-Cryst. Solids*, 1993, **159**, 1-21.
47. D. W. Matson, S. K. Sharma and J. A. Philpotts, *Am. Mineral.*, 1986, **71**, 694-704.
48. B. J. Riley, J. Chun, J. V. Ryan, J. Matyas, X. H. S. Li, D. W. Matson, S. K. Sundaram, D. M. Strachan and J. D. Vienna, *Rsc Advances*, 2011, **1**, 1704-1715.
49. B. O. Mysen and P. Richet, *Silicate glasses and melts*, Elsevier, 2018.
50. L. Cormier, D. Meneses, D. Neuville and P. Echegut, *Phys. Chem. Glass- B*, 2006, **47**, 430-434.
51. A. Deshkar, J. Marcial, S. A. Southern, L. Kobera, D. L. Bryce, J. S. McCloy and A. Goel, *J. Am. Ceram. Soc.*, 2017, **100**, 2859-2878.
52. J. Marcial, J. Kabel, M. Saleh, N. Washton, Y. Shaharyar, A. Goel and J. S. McCloy, *J. Am. Ceram. Soc.*, 2018, **101**, 2840-2855.
53. T. K. Bechgaard, A. Goel, R. E. Youngman, J. C. Mauro, S. J. Rzoska, M. Bockowski, L. R. Jensen and M. M. Smedskjaer, *J. Non-Cryst. Solids*, 2016, **441**, 49-57.
54. S. K. Lee and J. F. Stebbins, *Geochim. Cosmochim. Acta*, 2003, **67**, 1699-1709.
55. J. Wu and J. F. Stebbins, *J. Non-Cryst. Solids*, 2009, **355**, 556-562.
56. S. K. Lee, G. D. Cody, Y. Fei and B. O. Mysen, *Chem. Geol.*, 2006, **229**, 162-172.

57. A. Quintas, T. Charpentier, O. Majerus, D. Caurant, J. L. Dussossoy and P. Vermaut, *Appl. Magn. Reson.*, 2007, **32**, 613-634.
58. K.J.D. MacKenzie and M. E. Smith, *Multinuclear Solid-State NMR of Inorganic Materials*, Pergamon, Amsterdam, 2002.
59. H. Koller, G. Engelhardt, A. P. Kentgens and J. Sauer, *J. Phys. Chem.*, 1994, **98**, 1544-1551.
60. I. D. Brown and D. Altermatt, *Acta Crystallogr. B-Struct. Sci.*, 1985, **41**, 244-247.
61. J. W. Zwanziger, R. E. Youngman and S. L. Tagg, *J. Non-Cryst. Solids*, 1995, **192-193**, 157-160.
62. A. M. George and J. F. Stebbins, *Phys. Chem. Miner.*, 1996, **23**, 526-534.
63. D. A. McKeown, G. A. Waychunas and G. E. Brown, *J. Non-Cryst. Solids*, 1985, **74**, 325-348.
64. D. R. Neuville, L. Cormier, A. M. Flank, R. J. Prado and P. Lagarde, *Eur. J. Mineral.*, 2004, **16**, 809-816.
65. H. R. Fernandes, S. Kapoor, Y. Patel, K. Ngai, K. Levin, Y. Germanov, L. Krishtopa, S. Kroeker and A. Goel, *J. Non-Cryst. Solids*, 2018, **502**, 142-151.
66. S. Kapoor, R. E. Youngman, K. Zakharchuk, A. Yaremchenko, N. J. Smith and A. Goel, *J. Phys. Chem. B*, 2018, **122**, 10913-10927.
67. M. J. Toplis, D. B. Dingwell, K.-U. Hess and T. Lenci, *Am. Mineral.*, 1997, **82**, 979-990.
68. C. Angell, in *Relaxations in complex systems*, eds. K. L. Ngai and G. B. Wright, U.S. Department of Commerce National Technical Information Service, Springfield, Virginia, 1985, pp. 3-11.
69. C. A. Angell, K. L. Ngai, G. B. McKenna, P. F. McMillan and S. W. Martin, *J. Appl. Phys.*, 2000, **88**, 3113-3157.
70. Q. Zheng, M. Potuzak, J. C. Mauro, M. M. Smedskjaer, R. E. Youngman and Y. Yue, *J. Non-Cryst. Solids*, 2012, **358**, 993-1002.
71. M. M. Smedskjaer, J. C. Mauro, S. Sen and Y. Z. Yue, *Chem. Mater.*, 2010, **22**, 5358-5365.
72. D. R. Neuville, *Chem. Geol.*, 2006, **229**, 28-41.
73. J. F. Stebbins, E. V. Dubinsky, K. Kanehashi and K. E. Kelsey, *Geochim. Cosmochim. Acta*, 2008, **72**, 910-925.
74. S. A. Utlak and T. M. Besmann, *J. Chem. Thermodyn.*, 2019, **130**, 251-268.
75. J. C. Mauro, Y. Z. Yue, A. J. Ellison, P. K. Gupta and D. C. Allan, *Proceedings of the National Academy of Sciences of the United States of America*, 2009, **106**, 19780-19784.
76. Y. Shaharyar, J. Y. Cheng, E. Han, A. Maron, J. Weaver, J. Marcial, J. S. McCloy and A. Goel, *J. Am. Ceram. Soc.*, 2016, **99**, 2306-2315.
77. R. L. Withers, J. G. Thompson, A. Melnitchenko and S. R. Palethorpe, *Acta Crystallogr. B: Struct. Sci.*, 1998, **54**, 547-557.
78. X. Xue and J. F. Stebbins, *Phys. Chem. Miner.*, 1993, **20**, 297-307.
79. J. F. Stebbins, I. Farnan, E. H. Williams and J. Roux, *Phys. Chem. Miner.*, 1989, **16**, 763-766.
80. J. G. Thompson, P. J. R. Uwins, A. K. Whittaker and I. D. R. Mackinnon, *Clay. Clay Miner.*, 1992, **40**, 369-380.
81. G. L. Hovis, D.R. Spearing, J. F. Stebbins, J. Roux, A. Clara, *Am. Minerl.*, 1992, **77**, 19-29.
82. J. McCloy, N. Washton, P. Gassman, J. Marcial, J. Weaver and R. Kukkadapu, *J. Non-Cryst. Solids*, 2015, **409**, 149-165.
83. J. Marcial, J. Crum, O. Neill and J. McCloy, *Am. Mineral.*, 2016, **101**, 266-276.

84. N. Stone-Weiss, E. M. Pierce, R. E. Youngman, O. Gulbiten, N. J. Smith, J. Du and A. Goel, *Acta Biomater.*, 2018, **65**, 436-449.
85. P. K. Gupta, M. L. Lur and P. J. Bray, *J. Am. Ceram. Soc.*, 1985, **68**, C-82-C-82.
86. F. Angeli, O. Villain, S. Schuller, T. Charpentier, D. de Ligny, L. Bressel and L. Wondraczek, *Phys. Rev. B*, 2012, **85**, 054110.
87. R. Klingenberg, J. Felsche and G. Miehe, *J. Appl. Crystallogr.*, 1981, **14**, 66-68.
88. M. J. Buerger, G. E. Klein and G. Hamburger, *Geol. Soc. Am. Bull.*, 1946, **57**, 1182-1183.
89. G. Adam and J. H. Gibbs, *J. Chem. Phys.*, 1965, **43**, 139-146.
90. M. J. Toplis, *Am. Mineral.*, 1998, **83**, 480-490.
91. M. J. Toplis, *Chem. Geol.*, 2001, **174**, 321-331.
92. P. K. Gupta and J. C. Mauro, *J. Chem. Phys.*, 2009, **130**, 094503.
93. J. W. P. Schmelzer, A. S. Abyzov, V. M. Fokin, C. Schick and E. D. Zanotto, *J. Non-Cryst. Solids*, 2015, **428**, 68-74.
94. M. L. F. Nascimento and E. D. Zanotto, *J. Chem. Phys.*, 2010, **133**.
95. M. D. Ediger, P. Harrowell and L. Yu, *J. Chem. Phys.*, 2008, **128**.
96. J. Jiusti, E. D. Zanotto, D. R. Cassar and M. R. B. Andreeta, *J. Am. Ceram. Soc.*, 2020, **103**, 921-932.

Figure captions

Figure 1. Raman spectra of glasses of (a) SB-series and (b) BA-series

Figure 2. ^{23}Na MAS NMR spectra (a) SB-series and (b) BA-series glasses

Figure 3. 2D ^{23}Na MQ MAS NMR spectra of glasses (a) BL, (b) SB-10, (c) SB-20, (d) BA-10 and (e) BA-20. The minor contours to the top and bottom of the central contours are from spinning sidebands.

Figure 4. ^{11}B MAS NMR spectra (a) SB-series and (b) BA-series glasses

Figure 5 Viscosity data of selective glasses plotted on a T_g/T scale. The fragility m is calculated according to Angell's definition

Figure 6. Fragility values obtained from viscosity measurements and NBO/T values obtained from MAS-NMR data plotted against mol.% B_2O_3

Figure 7. X-ray diffractograms of glass samples non-isothermally heat-treated at 10 K/min and air quenched at various temperatures – (a) SB-series samples air-quenched at their respective onset of crystallization temperatures, (b) SB-series samples air-quenched at 1120 °C, (c) BA-series samples air-quenched at their respective onset of crystallization temperatures and (d) BA-series samples air-quenched in the temperature range of 840 – 1000 °C. The onset of crystallization temperature in these experiments is considered to be the temperature at which crystallinity is detected in the XRD, and is different than T_c obtained from the DSC.

Figure 8. Quantitative XRD analysis results of isothermally heat-treated samples (a) SB-series glasses heated at 950 °C for 24 h and (b) BA-series samples heated at 850 °C for 24 h

Figure 9. Estimation of liquidus viscosity of BA-10 by use of MYEGA model on viscosity values obtained by rotational viscometry and beam-bending method

Figure 10. X-ray diffractograms of the sample obtained from the cold end of the product obtained after the liquidus temperature measurement.

Figure 11. ^{23}Na MAS NMR spectra of the isothermally heat-treated glasses from (a) SB-series and (c) BA-series, and MAS projections of ^{23}Na MQMAS NMR spectra of the isothermally heat-treated glasses from (b) SB-series and (d) BA-series

Figure 12. ^{11}B MAS NMR spectra showing a comparison between glass and glass-ceramic obtained from isothermal heat-treatment of (a) SB-10, (b) SB-20, (c) BA-10 and (d) BA-20

Table 1. Batched vs. analyzed compositions of the studied glasses.

		Compositions								
		BL	SB-5	SB-10	SB-15	SB-20	BA-5	BA-10	BA-15	BA-20
Na_2O	mol.% (batched)	25.00	25.00	25.00	25.00	25.00	25.00	25.00	25.00	25.00
	mol.% (analyzed)	24.44	25.10	24.87	25.22	25.21	24.71	25.46	25.29	24.83
	wt.% (batched)	21.82	21.67	21.53	21.39	21.25	22.32	22.86	23.42	24.00
	wt.% (analyzed)	21.2	21.4	21.2	21.3	21.3	21.8	22.8	23.2	23.4
Al_2O_3	mol.% (batched)	25.00	25.00	25.00	25.00	25.00	20.00	15.00	10.00	5.00
	mol.% (analyzed)	26.21	26.17	26.25	26.28	26.55	21.02	16.02	10.80	5.50
	wt.% (batched)	35.89	35.65	35.41	35.18	34.95	29.38	22.56	15.41	7.90
	wt.% (analyzed)	37.4	36.7	36.8	36.5	36.9	30.5	23.6	16.3	8.53
B_2O_3	mol.% (batched)	0.00	5.00	10.00	15.00	20.00	5.00	10.00	15.00	20.00
	mol.% (analyzed)	0.00	5.05	9.54	14.65	19.29	4.80	9.66	14.75	19.65
	wt.% (batched)	0.00	4.87	9.67	14.41	19.09	5.02	10.27	15.78	21.57
	wt.% (analyzed)	0.00	4.84	9.13	13.9	18.3	4.76	9.72	15.2	20.8
SiO_2	mol.% (batched)	50.00	45.00	40.00	35.00	30.00	50.00	50.00	50.00	50.00
	mol.% (analyzed)	49.35	43.68	39.34	33.84	28.94	49.47	48.85	49.15	50.02
	wt.% (batched)	42.29	37.81	33.39	29.02	24.71	43.28	44.31	45.40	46.53
	wt.% (analyzed)	41.5	36.1	32.5	27.7	23.7	42.3	42.4	43.7	45.7

Table 2. Assignment of bands in the Raman spectra of SB- and BA-series glasses.

Wavenumber (cm^{-1})	Raman assignments
Region I	
448	Stretching-bending vibrations of T-O-T in five- or six-membered rings
490	T-O-T vibrations in four-membered rings (D1 defect band)
560	T-O-T breathing vibrations in three-membered rings (D2 defect band)
630	Danburite-like borosilicate rings
Region II	
700 to 850	T-O-T bending modes or motion of Si atom; T–O stretching vibrations involving oxygen motions in the T-O-T plane; chain-type metaborate groups
Region III	
935, 1000, 1120	Symmetric and asymmetric vibrations in fully polymerized tetrahedral $Si(OAl)_x$ units
Region IV	
1290, 1420, 1460	B-O stretching vibrations in borate units

Table 3. Estimated values of Na-O bond length and sodium coordination number *n* using isotropic chemical shift of ^{23}Na MAS NMR signal.

	δ_{CS} (ppm) (± 1 ppm)	Na-O bond length (Å) (± 0.02 Å)	shift parameter, A (± 0.1)	CN, *n* (± 0.2)
BL	-4.1	2.677	0.835	8.01
SB-10	-4.4	2.682	0.838	8.08
SB-20	-4.2	2.679	0.836	8.03
BA-10	-3.8	2.672	0.833	7.95
BA-20	-3.5	2.667	0.831	7.89

Table 4. $\%BO_3$ and $\%BO_4$ and NBOs per tetrahedron values calculated for SB-series and BA-series glasses as extracted from ^{11}B MAS NMR (standard deviation: ± 1%).

Sample	**$\%BO_3$**	**$\%BO_4$**	**NBO/T**
SB-10	100	0	0
SB-20	99	1	0.0002
BA-10	68	32	0.157
BA-20	39	61	0.209

Table 5. Thermal parameters (in °C) – T_g^{DSC}, T_c, T_p, T_m obtained from DSC-heating curve and T_g^{vis}, which represents temperature corresponding to a viscosity of 10^{12} Pa.s.

Glass	T_g^{DSC}	T_c	T_{p1}	T_{p2}	T_m	ΔT	T_g/T_m	T_g^{vis}
BL	802 ± 1	924 ± 2	961 ± 2	--	1526 ± 1	121 ± 2	0.598	808.9
SB-5	704 ± 2	810 ± 4	866 ± 2	971 ± 1	1290 ± 0	106 ± 4	0.625	--
SB-10	635 ± 2	787 ± 1	839 ± 2	922 ± 3	1231 ± 3	152 ± 2	0.604	629.1
SB-15	577 ± 2	790 ± 4	923 ± 5	--	1130 ± 4	213 ± 4	0.606	--
SB-20	541 ± 5	773 ± 7	877 ± 5	--	1044 ± 2	232 ± 9	0.618	542.3
BA-5	596 ± 2	707 ± 2	726 ± 1	--	--	112 ± 2	--	--
BA-10	538 ± 2	689 ± 1	729 ± 1	--	--	151 ± 3	--	535.5
BA-15	529 ± 1	--	--	--	--	--	--	--
BA-20	538 ± 1	--	--	--	--	--	--	525.3

Table 6. Summary of liquidus temperatures T_L, viscosity at liquidus temperatures (as per MYEGA fitting of viscosity data) and crystal phase at the liquidus (Standard deviation in T_L: ± 5 °C

	T_L (°C)	Viscosity at T_L (log_{10}Pa.s)	Crystal phase at liquidus
BL	1534	1.66	$Na_{1.15}Al_{1.15}Si_{0.85}O_4$ (cubic-carnegieite)
SB-10	1278	2.00	$Na_{1.15}Al_{1.15}Si_{0.85}O_4$ (cubic-carnegieite)
SB-20	1043	2.43	$Na_{7.15}Al_{7.2}Si_{8.8}O_{32}$ (Si-rich nepheline)
BA-10	994	2.85	$Na_{7.15}Al_{7.2}Si_{8.8}O_{32}$ (Si-rich nepheline)

Table 7. Calculated B_e/S_c values at T_g of selective glasses using Adam Gibb's equation. $Log_{10}\eta_{Tg}$ = 12.

Sample	T_g (K)	$Log_{10}\eta_\infty$ (log_{10}Pa.s)	$Log_{10}\eta_{Tg}$ - $Log_{10}\eta_\infty$ (log_{10}Pa.s)	B_e/S_c ((log_{10}Pa.s).K)
BL	1075.8	-3.37	15.37	16536.1
SB-10	908.2	-3.50	15.50	14078.9
SB-20	814.2	-1.89	13.89	11311.7
BA-10	811.3	-0.56	12.56	10187.5
BA-20	810.7	-0.73	12.73	10320.2

Table 8. Estimated temperatures for decoupling of viscosity and diffusion, T_d, and estimated glass-forming ability (GFA) parameter, $\eta(T_L)/T_L^2$

Sample	T_g (°C)	Estimated T_d (°C) = 1.15 – 1.25 * T_g	$\eta(T_L)/T_L^2$ (Pa.s/K^2)
BL	802.7	964-1071	1.39×10^{-5}
SB-10	635.1	771-862	4.16×10^{-5}
SB-20	541.1	663-744	1.55×10^{-4}
BA-10	538.2	660-741	4.41×10^{-4}
BA-20	537.6	659-740	--

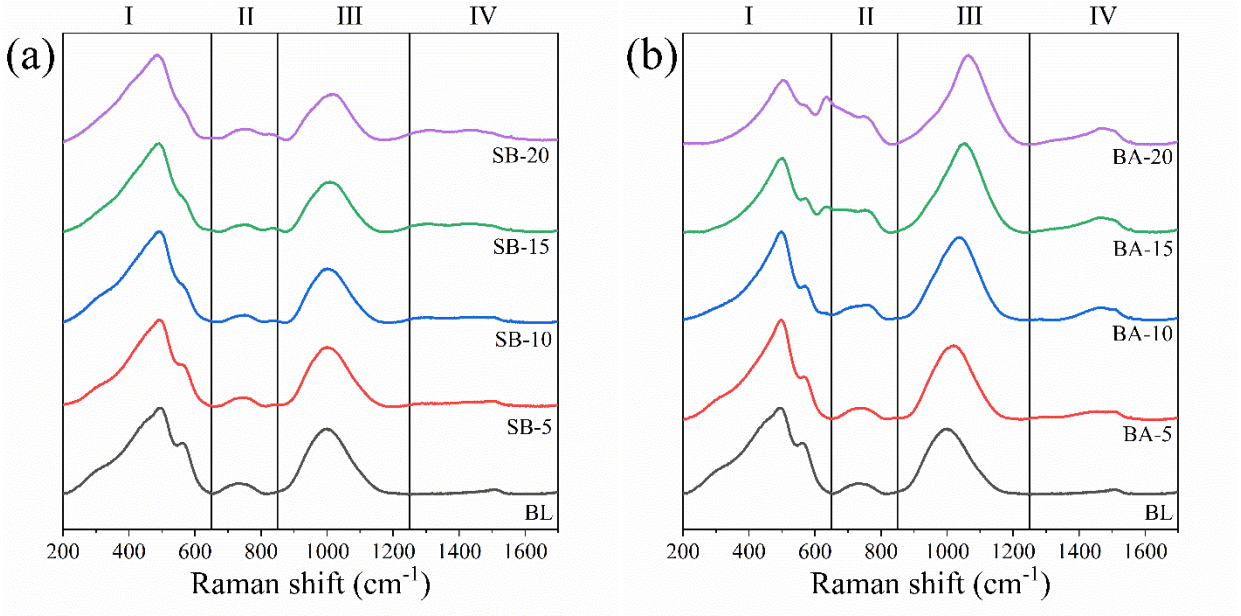

Figure 1. Raman spectra of glasses of (a) SB-series and (b) BA-series

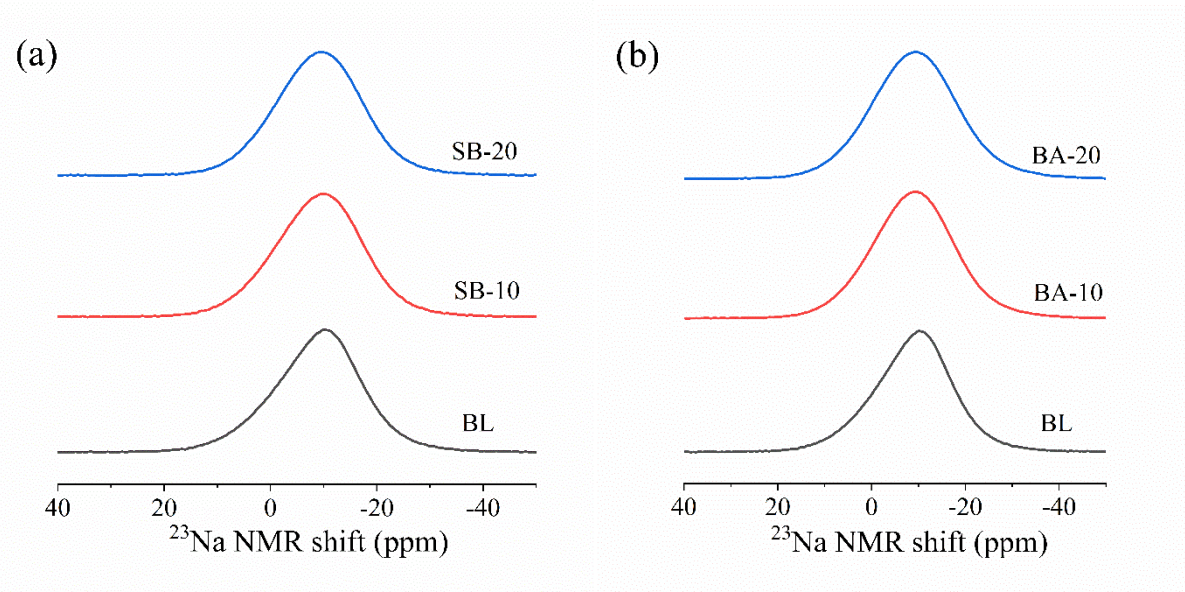

Figure 2. ^{23}Na MAS NMR spectra (a) SB-series and (b) BA-series glasses

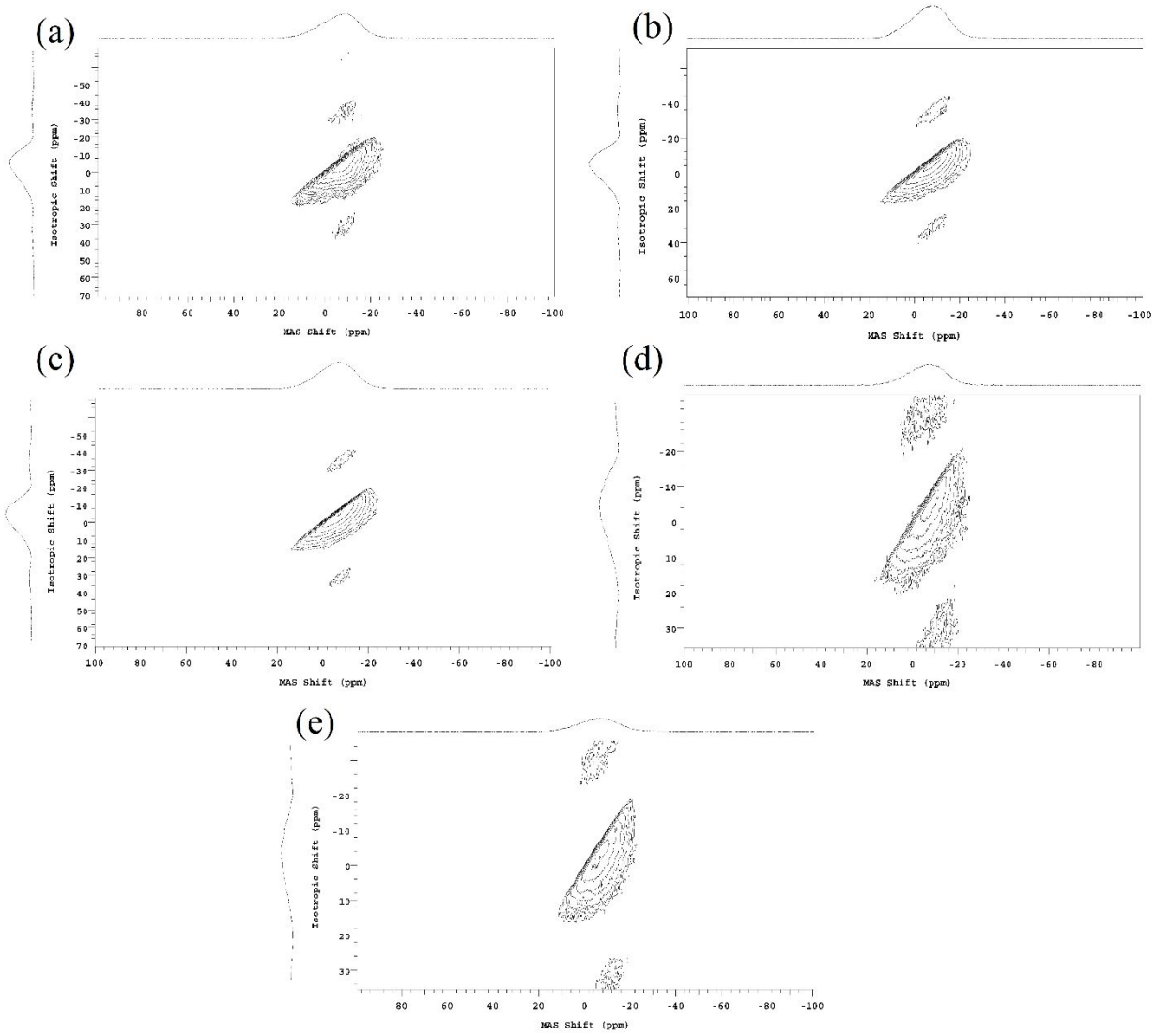

Figure 3. 2D ^{23}Na MQ MAS NMR spectra of glasses (a) BL, (b) SB-10, (c) SB-20, (d) BA-10 and (e) BA-20. The minor contours to the top and bottom of the central contours are from spinning sidebands.

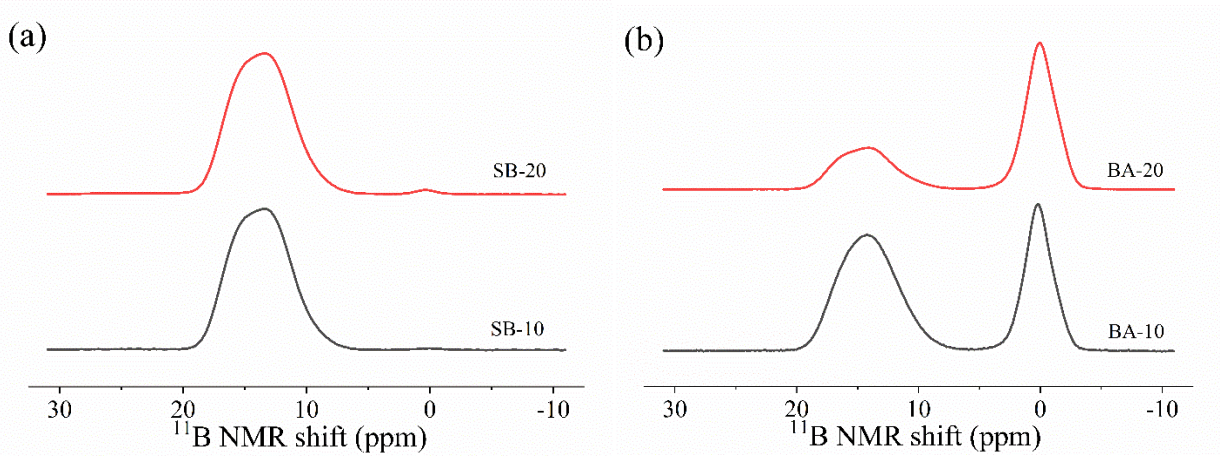

Figure 4. ^{11}B MAS NMR spectra (a) SB-series and (b) BA-series glasses

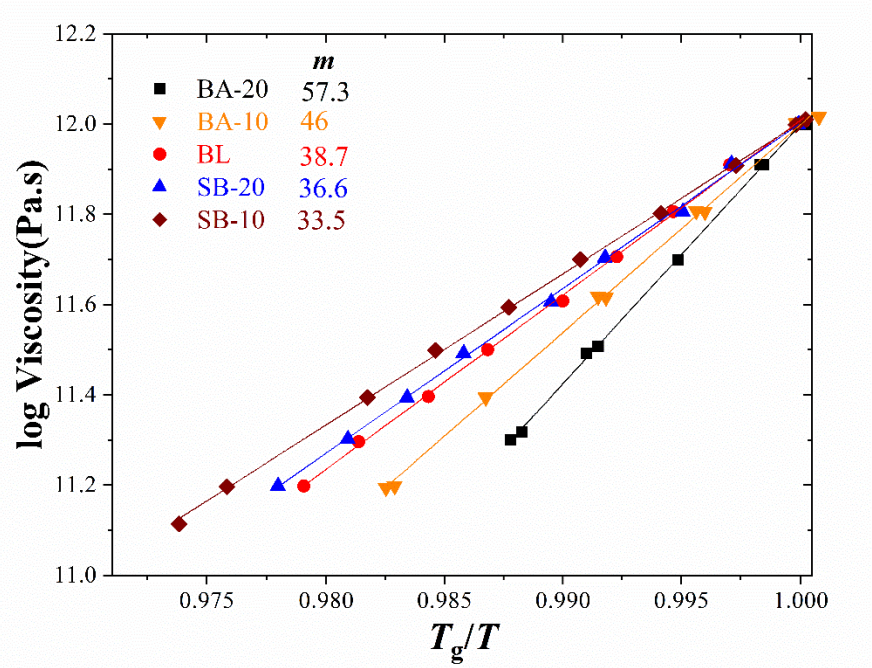

Figure 5. Viscosity data of selective glasses plotted on a T_g/T scale. The fragility m is calculated according to Angell's definition.

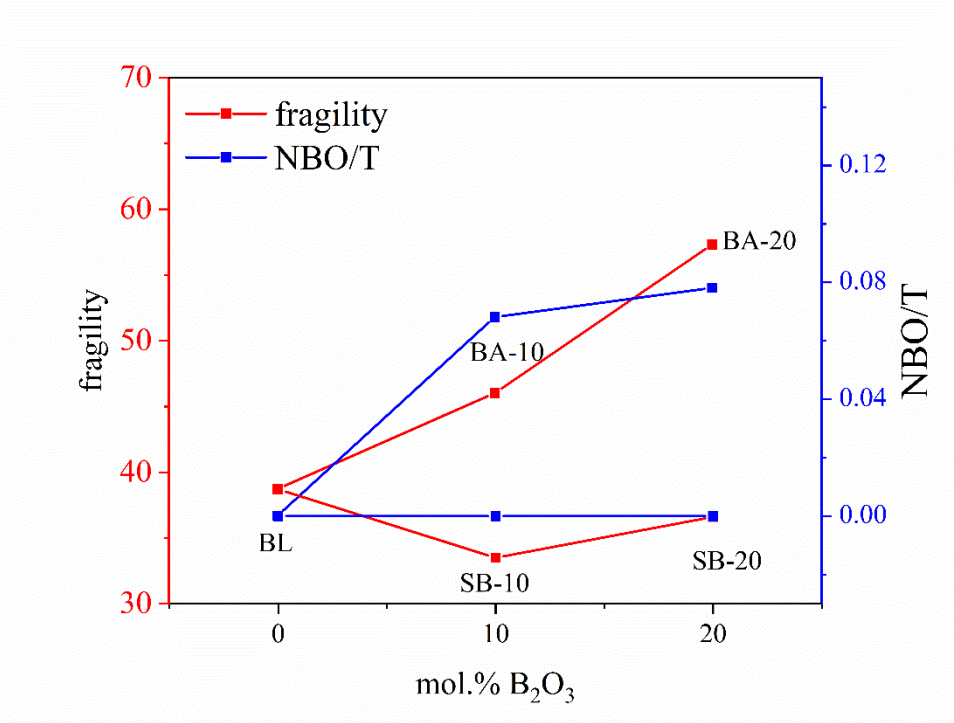

Figure 6. Fragility values obtained from viscosity measurements and NBO/T values obtained from MAS-NMR data plotted against mol.% B_2O_3

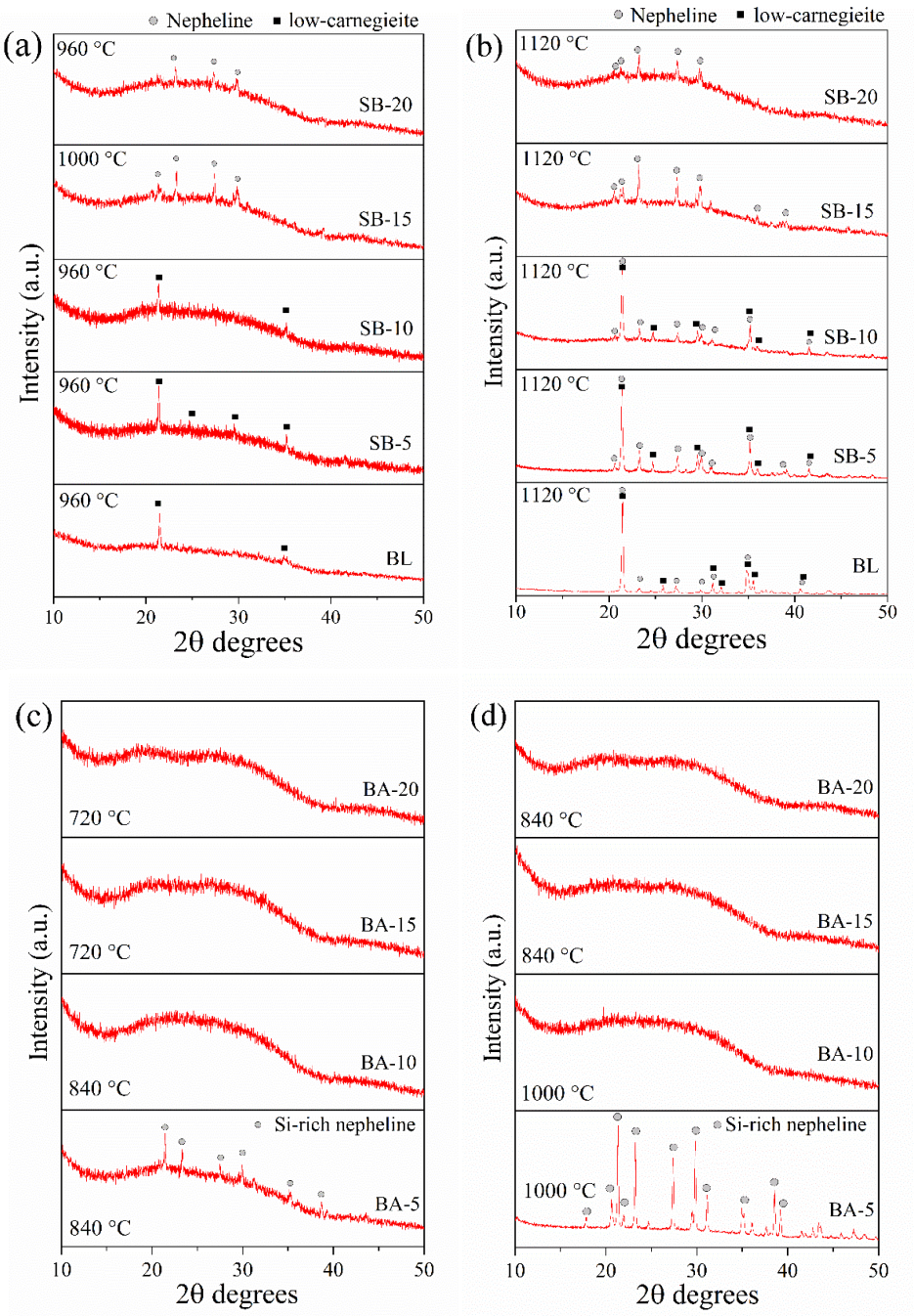

Figure 7. X-ray diffractograms of glass samples non-isothermally heat-treated at 10 K/min and air quenched at various temperatures – (a) SB-series samples air-quenched at their respective onset of crystallization temperatures, (b) SB-series samples air-quenched at 1120 °C, (c) BA-series samples air-quenched at their respective onset of crystallization temperatures and (d) BA-series samples air-quenched in the temperature range of 840 – 1000 °C. The onset of crystallization temperature in these experiments is considered to be the temperature at which crystallinity is detected in the XRD, and is different than T_c obtained from the DSC.

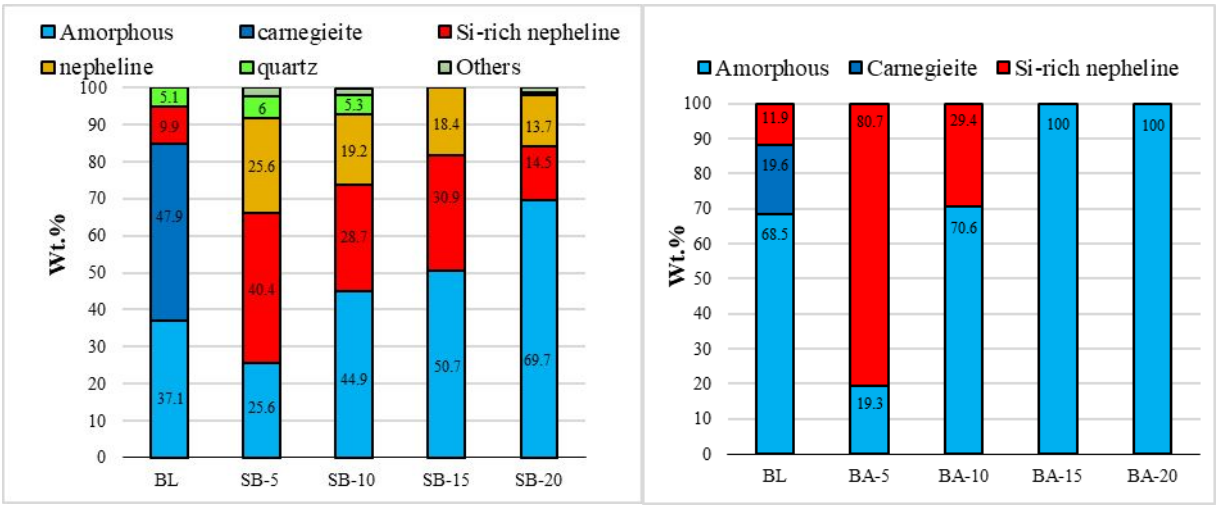

Figure 8. Quantitative XRD analysis results of isothermally heat-treated samples (a) SB-series glasses heated at 950 °C for 24 h and (b) BA-series samples heated at 850 °C for 24 h

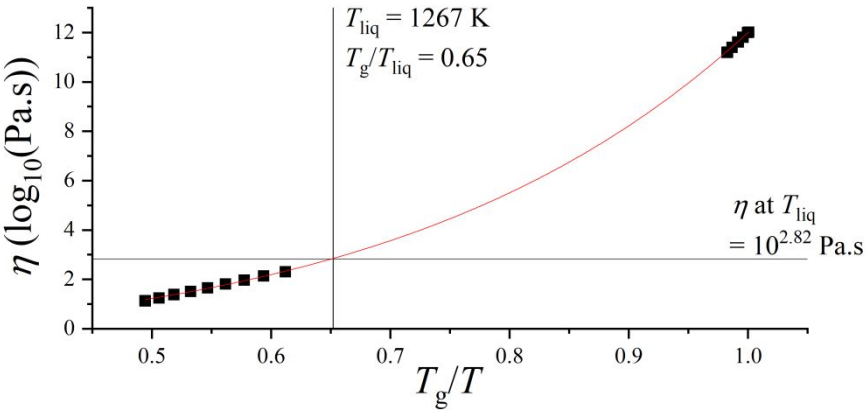

Figure 9. Estimation of liquidus viscosity of BA-10 by use of MYEGA model on viscosity values obtained by rotational viscometry and beam-bending method

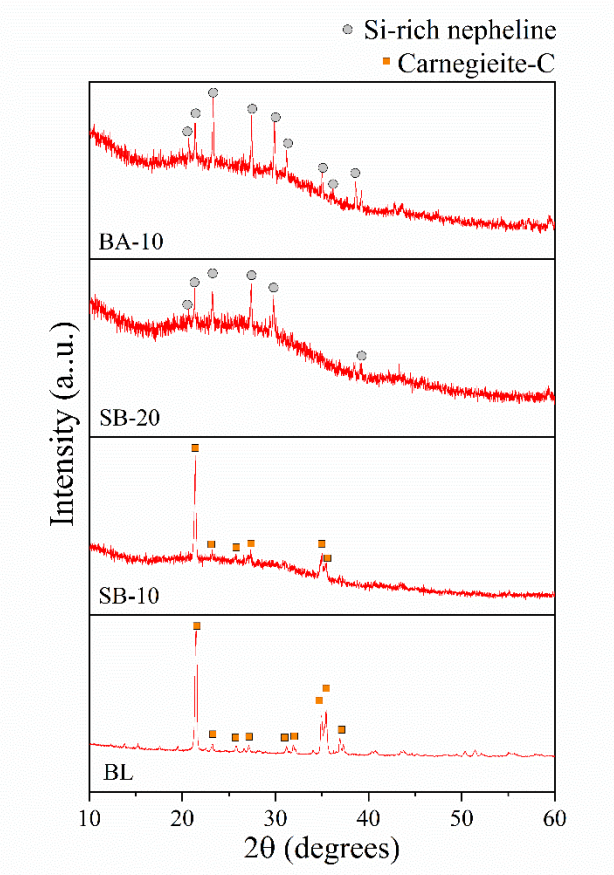

Figure 10. X-ray diffractograms of sample obtained from the cold end of product obtained after liquidus temperature measurement experiment

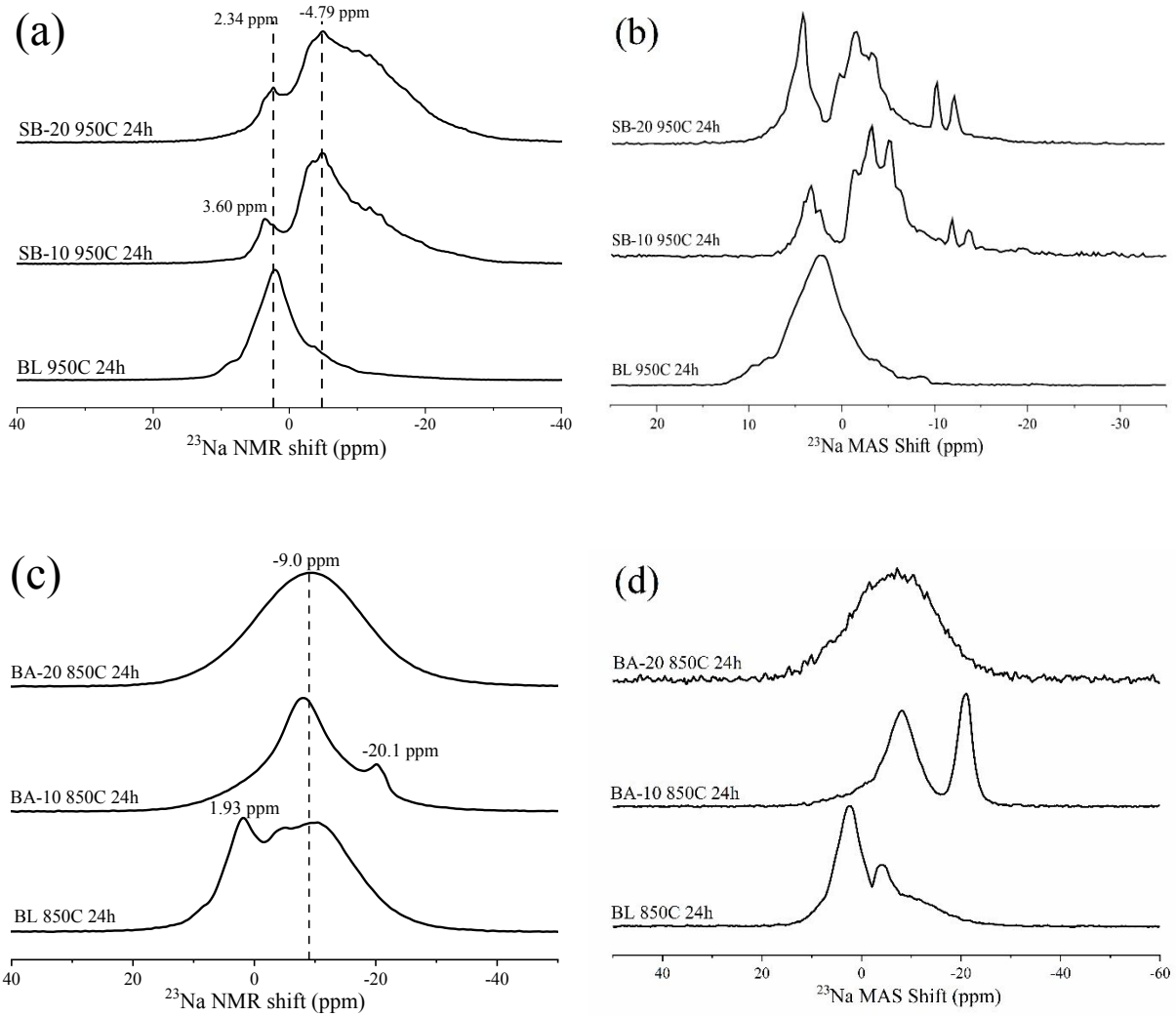

Figure 11. ^{23}Na MAS NMR spectra of the isothermally heat-treated glasses from (a) SB-series and (c) BA-series, and MAS projections of ^{23}Na MQMAS NMR spectra of the isothermally heat-treated glasses from (b) SB-series and (d) BA-series

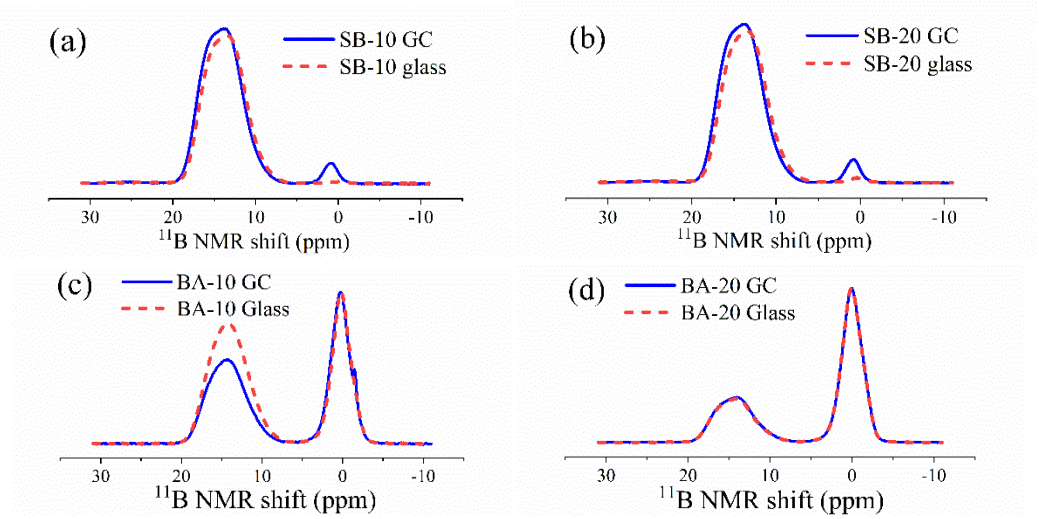

Figure 12. ^{11}B MAS NMR spectra showing a comparison between glass and glass-ceramic obtained from isothermal heat-treatment of (a) SB-10, (b) SB-20, (c) BA-10 and (d) BA-20